Wind Stress Vector over Ocean Waves

A. A. GRACHEV[*]

Cooperative Institute for Research in Environmental Sciences, University of Colorado, and NOAA/Environmental Technology Laboratory, Boulder, Colorado

C. W. FAIRALL

NOAA/Environmental Technology Laboratory, Boulder, Colorado

J. E. HARE

Cooperative Institute for Research in Environmental Sciences, University of Colorado, and NOAA/Environmental Technology Laboratory, Boulder, Colorado

J. B. EDSON

Woods Hole Oceanographic Institution, Woods Hole, Massachusetts

S. D. MILLER

Atmospheric Turbulence Laboratory, University of California, Irvine, Irvine, California

ABSTRACT

Previous investigations of the wind stress in the marine surface layer have primarily focused on determining the stress magnitude (momentum flux) and other scalar variables (e.g., friction velocity, drag coefficient, roughness length). However, the stress vector is often aligned with a direction different from that of the mean wind flow. In this paper, the focus is on the study of the stress vector direction relative to the mean wind and surface-wave directions. Results based on measurements made during three field campaigns onboard the R/P *Floating Instrument Platform* (*FLIP*) in the Pacific are discussed. In general, the wind stress is a vector sum of the 1) pure shear stress (turbulent and viscous) aligned with the mean wind shear, 2) wind-wave-induced stress aligned with the direction of the pure wind-sea waves, and 3) swell-induced stress aligned with the swell direction. The direction of the wind-wave-induced stress and the swell-induced stress components may coincide with, or be opposite to, the direction of wave propagation (pure wind waves and swell, respectively). As a result, the stress vector may deviate widely from the mean wind flow, including cases in which stress is directed across or even opposite to the wind.

1. Introduction

Determining the wind stress $\boldsymbol{\tau}$ (or momentum flux τ) over oceans is a fundamental problem of air–sea interaction. The stress vector exerted on the ocean surface is a key parameter for physical processes on both sides of the interface, including generation of the surface waves and local ocean currents. Decades of studies have

been done in determining the momentum flux over the ocean surface (e.g., Geernaert 1990; Smith et al. 1996).

The stress at the surface is the tangential force per unit area exerted by the wind on the surface. In practice the stress is usually measured by a sonic anemometer at a level of order 10 m above the sea surface. An elevated measurement of the stress is extrapolated to the surface, assuming that the stress is constant with height. The stress vector at some level well above the viscous sublayer measured via the eddy-correlation technique may be represented directly by the following relation:

$$\boldsymbol{\tau} = \boldsymbol{\tau}_x + \boldsymbol{\tau}_y = -\rho\langle u'w'\rangle\mathbf{i} - \rho\langle v'w'\rangle\mathbf{j}, \qquad (1)$$

where ρ is air density; $\mathbf{i}$ and $\mathbf{j}$ represent the longitudinal

* Additional affiliation: A. M. Obukhov Institute of Atmospheric Physics, Russian Academy of Sciences, Moscow, Russia.

Corresponding author address: Dr. Andrey A. Grachev, NOAA/ Environmental Technology Laboratory, R/ET6, 325 Broadway, Boulder, CO 80305-3328.
E-mail: andrey.grachev@noaa.gov

(x axis) and lateral (y axis) unit vectors; $\langle\ \rangle$ is a time and/or spatial averaging operator; u, v, and w are the longitudinal, lateral, and vertical (z axis) velocity components, respectively; and a prime denotes fluctuations about a mean value (e.g., $u = \langle u \rangle + u'$). In general, ($x$, y, z) is a fixed reference frame, although it is a common practice to align the x axis with wind direction at a reference height z. In this paper, we will hold the latter position; that is, in the general case, $\mathbf{i}$ is a function of z. Thus, the longitudinal stress component $\boldsymbol{\tau}_x = -\rho \langle u'w' \rangle \mathbf{i} \equiv \tau_x \mathbf{i}$ is the downstream stress, and the lateral stress component $\boldsymbol{\tau}_y = -\rho \langle v'w' \rangle \mathbf{j} \equiv \tau_y \mathbf{j}$ is the cross-wind stress. The following sign convention for stress is used: $\tau_x > 0$ if the longitudinal stress component is facing in the wind direction, and vice versa, and τ_y is positive (negative) if the lateral stress component is directed to the right (left) on the wind vector. Note that the stress vector defined above is that of the atmosphere on the ocean, that is, exerted by the wind on the surface. The stress of the ocean on the atmosphere is directed opposite to $\boldsymbol{\tau}$ according to Newton's third law.

The stress results in a transfer of horizontal momentum between the air and sea by the vertical momentum flux τ. Stress magnitude $|\boldsymbol{\tau}|$ is numerically equal to the magnitude of the momentum flux. For this reason, it is a common practice not to differentiate between stress and momentum flux. By convention, the momentum flux is defined to be positive downward (from atmosphere to ocean); that is, $\tau > 0$ that corresponds $\tau_x > 0$. In this case, waves extract momentum from the wind. Negative momentum flux corresponds to upward momentum transfer (from ocean to atmosphere); that is, $\tau_x < 0$. This regime is associated with the wave-driven wind (see also next section). The magnitude of the stress vector is given by

$$|\boldsymbol{\tau}| = \rho\sqrt{(\langle u'w' \rangle)^2 + (\langle v'w' \rangle)^2}. \qquad (2)$$

The angle α between the stress and wind vectors is calculated according to

$$\alpha = \arctan(\langle v'w' \rangle / \langle u'w' \rangle), \qquad (3)$$

where positive (negative) angles of α correspond to the stress vector oriented to the right (left) of the wind direction (left-handed coordinate system). Note that our definition of v' coincides with that of Gernaert (1988, 1996) and Rieder et al. (1994, 1996) but is opposite to Friehe et al. (2001). All directions for wind, waves, and stress in the paper are calculated using the meteorological convention (''from'').

The widely used friction velocity u_* is defined through stress magnitude as

$$u_*^2 = |\boldsymbol{\tau}|/\rho = \sqrt{(\langle u'w' \rangle)^2 + (\langle v'w' \rangle)^2}. \qquad (4)$$

The surface momentum flux is often estimated using a bulk method in which, by definition, τ is assumed to be proportional to a drag coefficient C_D and the square of the mean wind speed U ($U \equiv \langle u \rangle$),

$$\tau = \rho C_D U^2. \qquad (5)$$

In (5), both the wind speed and drag coefficient are representative of 10-m height above the surface. In most analyses to date, the direction of the stress vector is generally assumed to be aligned with the wind. The term $\langle v'w' \rangle$ in (1)–(4) is ignored on the assumption that it is unimportant or insignificant relative to $\langle u'w' \rangle$. The standard Monin–Obukhov similarity theory (MOST) and the drag coefficient parameterization (5) are based on the assumption that stress and wind vectors are aligned in the same direction, and $\langle v'w' \rangle = 0$ by definition. With the exception of several papers (see below), there has been a general lack of investigation concerning the stress vector direction relative to the mean wind and surface wave direction.

Smith (1980, p. 715) reported high values of the cross-wind component $\langle v'w' \rangle$, but these runs were rejected in subsequent data analysis. Based on aircraft measurements collected in the coastal zone off of northern California, Zemba and Friehe (1987, their Fig. 18) reported large angles between the stress and wind vectors at levels up to 1200 m. The observed departures of the stress vector direction from the wind direction can be associated with the presence of the coastal jet. Geernaert (1988) argued that the deviation of the stress vector from the wind vector is related to the surface heat flux and height above the surface. He suggested that the stress vector is directed to the left of the flow during stable stratification; for unstable stratification, it was to the right. According to MOST, the value of α in (3) should never exceed 5° in the absence of the thermal wind. In the Geernaert (1988) study, only 30% of the variance of α could be explained by air–sea heat flux, and it was suggested that the surface wave field (data unavailable in that study) could be responsible for some of the remaining variance of α. Based on a simple model, Geernaert (1996) argued that thermal advection and surface waves control α rather than heat flux. Based on the data obtained from a fixed research tower located 22 km offshore of the Virginia coast, Geernaert et al. (1993) found that the stress vector is governed, in large part, by the direction of swell. Geernaert et al. (1993) observed that, when swell propagates at an oblique direction with respect to the local wind direction, the stress vector is, in general, a blend between the wind direction and the swell direction. Geernaert et al. (1993) suggested that the mean orbital velocity vector can also be responsible for turning the surface wind stress away from the wind direction. Under this assumption, airflow separation induced by wave breaking could also affect the stress vector direction.

Rieder et al. (1994), using data collected on the R/P *Floating Instrument Platform* (*FLIP*) moored about 500 km west offshore of California, considered the influence of the surface waves on wind stress direction. They provided statistically more significant evidence that the wind stress lies between the mean wind direction and direction of the long waves, and they performed frequency analysis of the wind stress direction and waves

direction. Rieder et al. (1996) find that the direction of the wind stress and the whitecap motion are observed to be generally colinear, with both lying between the mean wind and the swell. Hwang and Shemdin (1988) previously reported that the primary direction of short-wave propagation is not aligned in the wind direction in the presence of swell. Although Hwang and Shemdin (1988) did not provide stress vector measurements, one may assume that the orientation of the surface stress is controlled by small-scale surface waves (see discussion below). Rieder and Smith (1998) extended their previous analysis of the wind stress vector over ocean waves, including frequency decomposition of the stress to remove surface wave effects. Wavelet analysis of the wind, stress, and wave data presented by Liu et al. (1995) showed the modulation of the wind component aligned with swell direction. As a result, the direction of the wind stress is affected by the underlying swell field. Recent progress on the influence of swell and other factors on the drag (5) and on the directional difference among the stress, wind, and the wave propagation is discussed by Donelan and Dobson (2001), and Friehe et al. (2001).

It is important to know the principal direction of short waves, because radar backscatter is sensitive to the direction their propagation (the ocean surface roughness). Rufenach et al. (1998) compared *European Remote Sensing Satellite* (*ERS*)-*1* spacecraft microwave scatterometer measurements with buoy wind data obtained at midlatitudes and the equatorial Pacific during 1992–94. They found that the mean wind direction derived from the scatterometer cross section is in good agreement with the buoy wind measurements at midlatitudes; however, there is a systematic directional offset near 10° in the equatorial region. According to Rufenach et al. (1998), the cross-sectional directional offset is most likely caused by swell propagating at large angles to the prevailing easterly winds across the equatorial Pacific Ocean. They suggest that the radar cross section is probably more closely related to the surface stress than to the wind velocity, because in the swell regime a stress direction is located between the mean wind and the long-wave direction. This viewpoint was confirmed by Cornillon and Park (2001) based on the wind vector field derived from the National Aeronautics and Space Administration Scatterometer (NSCAT) over Gulf Stream warm-core rings. Observations on Lake Ontario made by Colton et al. (1995) showed that the behavior of the normalized radar cross section for microwave backscatter from a wind-roughened surface is more consistent with a dependence on wind stress than on wind speed. This conclusion is based on the analysis of the stress magnitude (4), or (5), rather than on the stress direction (3).

Some aspects of waves running at an angle to the wind direction based on turbulence closure modeling have been examined by Li et al. (2000). Mahrt et al. (2001) recently discussed departures of the stress vector direction from the wind direction above land. They argue that the value of α in (3) is largest for very unstable conditions and reaches about 25° for $z/L = -2$ (L is the Obukhov length). In addition, the value of α is also influenced by baroclinity, nonstationarity, and large entrainment of momentum during rapid boundary layer growth periods, as well as by the method of averaging. Based on the Microfronts data collected in Kansas during March 1995, Mahrt et al. (2001) show that the stress vector is rotated clockwise, consistent with the Ekman turning of the wind vector. This is also consistent with Geernaert's (1988) prediction for unstable stratification.

The Geernaert (1988), Geernaert et al. (1993), and Rieder et al. (1994, 1996) studies restricted their analyses to moderate to high wind speeds (above 3 m s^{-1}). In light wind speed regimes, the influence of the surface waves on wind stress direction is more dramatic. It is commonplace that, in calm weather conditions, the wind and stress vectors are not aligned (e.g., Mahrt et al. 1996), and often the wind and stress directions are nearly opposite (Drennan et al. 1999). However, these cases were treated as sampling uncertainties or even nonphysical results (Rieder et al. 1994). During light winds, angles between the wind and stress directions are distributed randomly. According to Drennan et al. (1999, their Fig. 9), the stress vector may be oriented to the left of as well as to the right of the wind direction in weak wind conditions. One may argue that this scatter is associated with the small values of the stress and that stress measurements are relatively unreliable for weak winds.

Wind-wave tank measurements by Remy and Giovanangeli (1999) shows that in the presence of the steep long oblique wave, the constant shear layer near the surface can disappear and wind stress deviates from the wind direction toward the oblique wave. This deviation increases on approach to the water surface and with increasing of the oblique wave steepness. According to Remy and Giovanangeli (1999), at any height, the total stress appears as a combination of pure turbulent stress aligned with the wind, an oblique wave–induced stress aligned in the oblique wave direction, and a wind-wave stress aligned with the wind wave direction. Each contribution to the total stress depends upon the height and the steepness of the oblique longer wave. Moreover, in such conditions the inertial dissipation method and the eddy-correlation method can disagree.

Grachev and Fairall (2001) recently analyzed data from R/P *FLIP* and found that during light winds deviations of the stress vector direction from the wind vector are not random. They showed that the stress vector direction is governed by both the swell direction and the wind direction. For moderate and strong winds ($U \geq 5$–6 m s^{-1}), τ basically lies in the acute angle between the wind direction and the wave direction (cf. Geernaert et al. 1993; Rieder et al. 1994, 1996). In the case of light winds and background swell, the stress vector lies in the obtuse angle between the wind direction and the

opposite wave direction; that is, it is facing the opposite direction from the direction of wave propagation (see details in the next section). According to Grachev and Fairall (2001), the stress was generally observed to be left of the airflow (their Fig. 5b) for the conditions of the measurements. Because the stratification was unstable (their Fig. 2), this deviation appeared to be opposite to the predictions by Geernaert (1988) and Mahrt et al. (2001). Results obtained by Grachev and Fairall (2001) support the view by Geernaert et al. (1993) and Rieder et al. (1994, 1996) that deviation of the stress from the wind direction over the sea is caused by waves rather than by thermal stratification (Geernaert 1988). Thus, one may conclude that the stratification effect on the value of α, [(3)] over the sea is insignificant with respect to the wave effect.

The purpose of this study is to extend these prior analyses by including additional experimental evidence of the influence of surface wave direction on the stress vector direction. Here, we consider the directional characteristics of the wind, stress, and surface waves during different meteorological situations including counter-swell cases and decaying sea state. Most of the data are simultaneous wind and stress measurements at several levels. The data used here were collected by the National Oceanic and Atmospheric Administration/Environmental Technology Laboratory (NOAA/ETL) and Woods Hole Oceanographic Institution (WHOI) during three R/P *FLIP* expeditions in 1993 and 1995.

2. Basic approach

The above discussion shows that, at the sea surface, the total stress tends to be governed by two vectors aligned with the wind and swell directions, respectively. It makes sense to decompose the surface stress vector in two vectors aligned with wind ($\boldsymbol{\tau}_1$) and swell ($\boldsymbol{\tau}_2$), respectively:

$$\boldsymbol{\tau} = \boldsymbol{\tau}_1 + \boldsymbol{\tau}_2. \qquad (6)$$

Figure 1 shows a decomposition of the stress vector in the traditional rectangular coordinate system, $\boldsymbol{\tau}_x$ and $\boldsymbol{\tau}_y$, and in the wind–swell coordinate system, $\boldsymbol{\tau}_1$ and $\boldsymbol{\tau}_2$ (θ_2 is a relative angle between the wind and swell). In fact, we replace a fixed rectangular Cartesian reference frame associated with the wind alone and used in (1) by a fixed nonrectangular reference frame associated with the wind and swell directions (6). Axes of this coordinate system are oriented in the wind direction and in the direction of the swell propagation, respectively. The relationships between stress components in these two coordinate systems are given by (see Fig. 1)

$$\tau_x = \tau_1 + \tau_2 \cos\theta_2 \quad \text{and} \quad \tau_y = \tau_2 \sin\theta_2, \quad \text{or}$$

$$\tau_1 = \tau_x - \tau_y \cot\theta_2 \quad \text{and} \quad \tau_2 = \tau_y/\sin\theta_2. \qquad (7)$$

Note that (6) and (7) are not useful in the case of $\sin\theta_2$

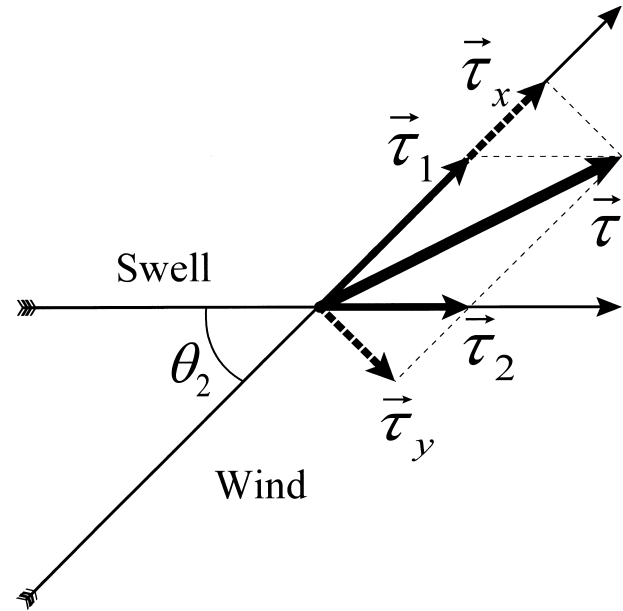FIG. 1. Decomposition of the stress vector $\boldsymbol{\tau}$ into $\boldsymbol{\tau}_x$ and $\boldsymbol{\tau}_y$ in a wind-associated coordinate system and into $\boldsymbol{\tau}_1$ and $\boldsymbol{\tau}_2$ in a wind–swell coordinate system.

$= 0$, when the wind is aligned with the swell (in the same or opposite direction).

Consider the physical reasons that cause a deviation of the stress from a wind direction over waves and, therefore, specify $\boldsymbol{\tau}_1$ and $\boldsymbol{\tau}_2$. Over the sea, the total stress $\boldsymbol{\tau}$ can be expressed as the vector sum of shear stress $\boldsymbol{\tau}_{\text{shear}}$ and wave-induced stress $\boldsymbol{\tau}_{\text{wave}}$ (e.g. Phillips 1977):

$$\boldsymbol{\tau}(z) = \boldsymbol{\tau}_{\text{shear}}(z) + \boldsymbol{\tau}_{\text{wave}}(z)$$

$$\equiv \boldsymbol{\tau}_{\text{visc}}(z) + \boldsymbol{\tau}_{\text{turb}}(z) + \boldsymbol{\tau}_{\text{wave}}(z), \qquad (8)$$

where $\boldsymbol{\tau}_{\text{shear}}(z)$ is the sum of viscous stress $\boldsymbol{\tau}_{\text{visc}}(z)$ and turbulent shear stress $\boldsymbol{\tau}_{\text{turb}}(z)$. The viscous stress is important only in the near-surface molecular sublayer. The total stress $\boldsymbol{\tau}$ beyond the viscous sublayer in the left side of (8) is given by (1). In general, all constituents in (8) depend on z. However, under certain conditions (the wind and wave fields are stationary in time and space), it is assumed that $\boldsymbol{\tau}$ in the left side of (8) is constant with height; that is, $\partial\boldsymbol{\tau}/\partial z \approx 0$. The amplitude of wave-induced pressure perturbations falls off exponentially with z (Hare et al. 1997), and, therefore, well away from the surface, $\boldsymbol{\tau}_{\text{wave}}(z)$ tends to zero. If one assumes that $\boldsymbol{\tau}$ is invariant with height (constant flux layer), changes of $\boldsymbol{\tau}_{\text{wave}}(z)$ with height must be compensated by variations of $\boldsymbol{\tau}_{\text{turb}}(z)$ and $\boldsymbol{\tau}_{\text{visc}}(z)$. The layer in which the influence of $\boldsymbol{\tau}_{\text{wave}}(z)$ cannot be neglected is known as the wave boundary layer (WBL). It is generally believed that above the WBL, but within the surface layer, the standard MOST is applicable for the description of the momentum transfer.

Separation of $\boldsymbol{\tau}$ above the wave surface into shear and wave-induced components, according to (8), results from

decomposition of the total wind velocity into three parts: mean, turbulent, and wave-induced components, or

$$u = \langle u \rangle + u' \equiv \langle u \rangle + u'_t + \tilde{u}, \tag{9}$$

where $(')$ denotes turbulent fluctuations and the tilde denotes wave-induced fluctuations. It is assumed that the wave-induced and turbulent components are uncorrelated. The corresponding relationships for v and w velocity components are derived in a similar manner by the simple replacement of the u symbol in (9) with v and w symbols. Notation $(')$ in (1) and (9) represents both turbulent fluctuations and the wave-induced component—that is, $u' = u'_t + \tilde{u}$. Note that measurement of the *total* stress defined by (1) is a straightforward application for a sonic anemometer. Thus, stress components in (8) above the sea surface can be expressed as (e.g., Hare et al. 1997)

$$\boldsymbol{\tau}_{\mathrm{visc}}(z) = \rho\nu\left(\frac{d\langle u \rangle}{dz}\mathbf{i} + \frac{d\langle v \rangle}{dz}\mathbf{j}\right),$$

$$\boldsymbol{\tau}_{\mathrm{turb}}(z) = -\rho(\langle u'_t w'_t \rangle \mathbf{i} + \langle v'_t w'_t \rangle \mathbf{j}), \quad \text{and}$$

$$\boldsymbol{\tau}_{\mathrm{wave}}(z) = -\rho(\langle \tilde{u}\tilde{w} \rangle \mathbf{i} + \langle \tilde{v}\tilde{w} \rangle \mathbf{j}), \tag{10}$$

where ν is the kinematic viscosity. In strict terms, the direction of both $\boldsymbol{\tau}_{\mathrm{turb}}(z)$ and $\boldsymbol{\tau}_{\mathrm{visc}}(z)$ is controlled by the shear vector, not the wind vector (i.e., $\mathbf{i}$). For this reason, the viscous stress and the turbulent stress in (10) contains components aligned with both $\mathbf{i}$ and $\mathbf{j}$. However, in many cases, direction of the shear vector coincides with the wind vector, and terms $(d\langle v \rangle/dz)\mathbf{j}$ and $\langle v'_t w'_t \rangle \mathbf{j}$ in (10) can be omitted. It is common practice (e.g., Makin and Kudryavtsev 1999) to relate $\boldsymbol{\tau}_{\mathrm{turb}}(z)$ to the gradient of the velocity field through the eddy viscosity in the same way as $\boldsymbol{\tau}_{\mathrm{visc}}(z)$ in (10).

On the sea surface $z = \eta$, the stress is composed of contributions from the viscous stress $\boldsymbol{\tau}_{\mathrm{shear}}(\eta) \approx \boldsymbol{\tau}_{\mathrm{visc}}(\eta)$ and surface wave–induced stress $\boldsymbol{\tau}_{\mathrm{wave}}(\eta)$. The surface wave–induced stress is often named normal stress (also, form stress or pressure drag). It is associated with the atmospheric pressure distribution across the front and rear faces of the wave and is described by $\boldsymbol{\tau}_{\mathrm{wave}i}(\eta) \approx \langle p(\partial\eta/\partial x_i)\rangle$ (where the spatial derivative defines the wave slope). In the case of a pure unimodal, one-dimensional wave field (e.g., Belcher and Hunt 1998; Sullivan et al. 2000), $\boldsymbol{\tau}_{\mathrm{wave}}(\eta)$ is aligned with the direction of wave propagation. The fundamental difference between airflow over land and sea derives from the mobility of the water surface. This phenomenon is traditionally described in terms of wave age, c_p/u_* or c_p/U, where c_p is the phase speed of the component in the peak of the spectrum. Using wave age, the sea state is classified into young (or developing) sea, $c_p/U < 1.2$, and mature (old) sea, $c_p/U > 1.2$ (Pierson and Moskowitz 1964; Donelan 1990). The wave-induced stress component in the marine surface layer shows strong dependence on wave age and ranges from positive to negative values (e.g., Makova 1975; Sullivan et al.

2000). For young seas, the wave-induced stress is positive. With increasing wave age, the wave-induced stress reaches zero, and it reverses sign in the case of old seas (e.g., Grachev and Fairall 2001). The fact that the wave-induced stress can be positive as well as negative is a key point to understanding the stress vector orientation over ocean waves.

The nature of real ocean waves is more complicated than the idealized wave field discussed above. Natural oceanic waves occur over a broad frequency band and extend from capillary to long gravity waves. It is generally assumed that surface gravity waves can be separated into pure wind-sea waves and swell waves. These waves are different in origin and differ in properties. Locally generated wind waves are generally short waves and travel much more slowly than the wind, whereas swell waves are long and fast-traveling ocean waves (e.g., Donelan and Dobson 2001). Wind-sea waves are generated by a local wind; swells are generated in other areas at other times. Short waves extract momentum from wind, and energy is conveyed to the surface-wind waves. With increasing duration and fetch, these waves reach equilibrium with the local wind field. Swells produced by a storm can travel thousands of kilometers, propagating into an observation region. Swells have a period and wavelength that are not associated with local winds. In the majority of cases, the wave energy of swell is contained in a narrow range around the peak frequency in the wave spectrum and is separated from the wave energy of wind-dominant waves. However, as a first approximation, one might consider that wind waves and swell are not correlated. Thus, it makes sense to split the surface wave–induced stress into two parts, $\boldsymbol{\tau}_{\mathrm{wave}}(\eta) = \boldsymbol{\tau}_{\mathrm{wave}1}(\eta) + \boldsymbol{\tau}_{\mathrm{wave}2}(\eta)$, where $\boldsymbol{\tau}_{\mathrm{wave}1}(\eta)$ and $\boldsymbol{\tau}_{\mathrm{wave}2}(\eta)$ are due to local wind waves and oceanic swell, respectively. Combining this assumption and (8) for $z = \eta$ yields

$$\boldsymbol{\tau}(\eta) = \boldsymbol{\tau}_{\mathrm{shear}}(\eta) + \boldsymbol{\tau}_{\mathrm{wave}1}(\eta) + \boldsymbol{\tau}_{\mathrm{wave}2}(\eta). \tag{11}$$

In general, wind waves and swell propagate in different directions (i.e., θ_1 and θ_2 are relative angles between the wind and wind waves and swell, respectively). However, for stationary conditions, the direction of wind waves is frequently close to the wind direction (e.g., Geernaert et al. 1993, their Table 1; Rieder et al. 1996, their Fig. 2; Rieder and Smith 1998, their Fig. 4), that is, $|\cos\theta_1| \approx 1$, and therefore vector $\boldsymbol{\tau}_{\mathrm{wave}1}(\eta)$ is aligned with the wind direction. This problem is complicated in nearshore regions, particularly if coastal topography is able to steer either wind or wave directions.

According to Rieder and Smith (1998), $\boldsymbol{\tau}_{\mathrm{wave}1}$ and $\boldsymbol{\tau}_{\mathrm{wave}2}$ are associated with different frequency bands. The swell-induced stress $\boldsymbol{\tau}_{\mathrm{wave}2}$ is controlled by the frequency band between 0.06 and 0.16 Hz and is biased toward the direction of long-period swell. Stress in the high-frequency band, $f > 0.16$ Hz, is associated with high-frequency equilibrium-range waves and is biased toward

the direction of short-period seas, which is close to the wind direction.

In the case of complex sea (mixed wind sea and swell), $\tau_{\mathrm{wave1}}(\eta)$ and $\tau_{\mathrm{wave2}}(\eta)$ are governed by their own wave age, $c_{p1}/U\cos\theta_1$ and $c_{p2}/U\cos\theta_2$, respectively (two peaks in the wave spectra are expected). Because the swell usually travels faster and short waves travel more slowly than the wind, in the majority of cases $\tau_{\mathrm{wave1}}(\eta) > 0$ and $\tau_{\mathrm{wave2}}(\eta) < 0$. However, reverse signs are also possible in transient conditions. Case $\tau_{\mathrm{wave1}}(\eta) < 0$ is associated with decaying wind conditions, after the passage of a storm or gale, when the total stress may reverse sign to negative, $\tau_x < 0$ (e.g., Kitaigorodskii 1970; Smedman et al. 1994). Case $\tau_{\mathrm{wave2}}(\eta) > 0$ is associated with strong winds traveling in the same direction as the swell or the counterswell and leads to enhancement of the total stress (e.g., Drennan et al. 1999; Donelan and Dobson 2001). Unlike the wave-induced stress, the surface shear stress is always positive—that is, $\tau_{\mathrm{shear}}(\eta) > 0$. The case $\tau_{\mathrm{shear}}(\eta) < 0$ is an exotic situation, and it could be associated with the nonzero sea surface velocity with the same direction as the wind (currents or wave orbital motions).

Specification of $\boldsymbol{\tau}_1(\eta)$ and $\boldsymbol{\tau}_2(\eta)$ in terms of the shear stress and wave-induced stress requires determination of their orientations. Wind-wave-induced stress $\boldsymbol{\tau}_{\mathrm{wave1}}(\eta)$ is aligned with the wind direction, and swell-induced stress $\boldsymbol{\tau}_{\mathrm{wave2}}(\eta)$ is governed by swell direction. Determination of the $\boldsymbol{\tau}_{\mathrm{shear}}(\eta)$ direction is not so obvious. As mentioned above, the shear vector is usually coincident with the mean wind direction, and therefore vectors $\boldsymbol{\tau}_{\mathrm{shear}}(\eta)$ and $\boldsymbol{\tau}_{\mathrm{wave1}}(\eta)$ are approximately codirectional. This results in

$$\boldsymbol{\tau}_1(\eta) = \boldsymbol{\tau}_{\mathrm{shear}}(\eta) + \boldsymbol{\tau}_{\mathrm{wave1}}(\eta) \quad \text{and}$$

$$\boldsymbol{\tau}_2(\eta) = \boldsymbol{\tau}_{\mathrm{wave2}}(\eta). \tag{12}$$

According to the above discussion, the wave-induced stress components, $\tau_{\mathrm{wave1}}(\eta)$ and $\tau_{\mathrm{wave2}}(\eta)$, can be positive as well as negative. As a result, according to (12), the vector $\boldsymbol{\tau}_1$ may face into the wind direction ($\tau_1 > 0$) or in the opposite direction ($\tau_1 < 0$). In a similar way, $\boldsymbol{\tau}_2$ may face into the swell direction ($\tau_2 > 0$) or against to the swell propagation ($\tau_2 < 0$). Combining these cases gives all possible situations associated with the stress direction. Some of these situations are prohibited; e.g., in counterswell cases $\tau_2(\eta)$ can be only negative. Figures 2 and 3 summarize these cases. We consider here a general case in which the wind and swell directions are not aligned. Figure 2 shows situations in which the wind has a component in the direction of swell propagation ($\cos\theta_2 > 0$). Figure 3 presents counterswell cases, when the projection of the wind vector is directed against swell direction ($\cos\theta_2 < 0$). Note that Figs. 1–3 are only schematic sketches, and all vectors are out of scale.

Figure 2a presents the typical case associated with moderate and strong winds or weak swells (this case

also shown in Fig. 1). Both vector components are positive, $\tau_1 > 0$ and $\tau_2 > 0$, and the total stress vector lies in the acute angle between the wind direction and the swell direction and is facing in the wind/wave direction. This case was described by Geernaert et al. (1993) and Rieder et al. (1994, 1996) in detail. As wind speed decreases, the swell-induced stress τ_2 decreases, reaches zero, and reverses sign but τ_1 is still positive. This case is shown in Fig. 2b, and it is associated with light winds and strong background swell (swell regime), $\tau_1 > 0$ and $\tau_2 < 0$. The stress vector in this case is within the obtuse angle created by the wind direction and the direction opposite to the swell propagation. This regime was reported by Grachev and Fairall (2001, their Fig. 5). In a particular case, the stress vector may be directed perpendicular to the wind ($\tau_x = 0$, but $\tau_y \neq 0$). The next two cases (Figs. 2c,d) are associated with decaying wind conditions ($\tau_1 < 0$ because of negative τ_{wave1}). In these situations, the wind speed drops in a short time period, but the local wind waves still travel with high phase velocities that lead to upward momentum transfer from ocean to atmosphere. The situation in Fig. 2c is associated with light winds, $\tau_2 < 0$. The stress vector in this case lies at an acute angle between directions opposite both to wind and swell. One may expect that the regime in Fig. 2c rarely occurs. It seems likely that the case in which $\tau_1 < 0$ and $\tau_2 > 0$ (Fig. 2d) is more improbable than the situation shown in Fig. 2c because 2d requires that wind speed be high enough to satisfy the condition $\tau_2 > 0$ but at the same time have a decaying wind regime.

In cases in which the wind blows against the swell (Fig. 3), waves always drag the airflow and extract energy. Therefore, a stress component is always directed against the swell direction regardless of the wind speed magnitude, $\tau_2(\eta) < 0$. The situation shown in Fig. 3a is a regular case associated with steady-state wind conditions, whereas the case in Fig. 3b is a decaying-wind regime. Figure 3a clearly reveals an enhancement of the total stress for the counterswell runs reported early by Donelan et al. (1997) and Drennan et al. (1999).

The conceptual scheme discussed above is derived for the stress at the wavy surface, $z = \eta$, although (6)–(7) as well as the vector balance in Figs. 1–3 are valid at any height withing the WBL. However, the extrapolation of the surface stress to the elevated measurements is not a trivial problem [see discussion in Hare et al. (1997)]. Neither $\tau_{\mathrm{wave1}}(z)$ nor $\tau_{\mathrm{wave2}}(z)$ are described by a simple exponentially decaying profile; they have a more complicated nonmonotonic structure. In laboratory flows (Stewart 1970; Hsu et al. 1981; Hsu and Hsu 1983) and field measurements (Hare et al. 1997; Wetzel 1996), as well as in theoretical treatments (Townsend 1972), it was found that the wave-induced stress may reverse sign with height several times. Thus, the various constituents on the right side of (8) vary with height in different ways. A comparison of the approach
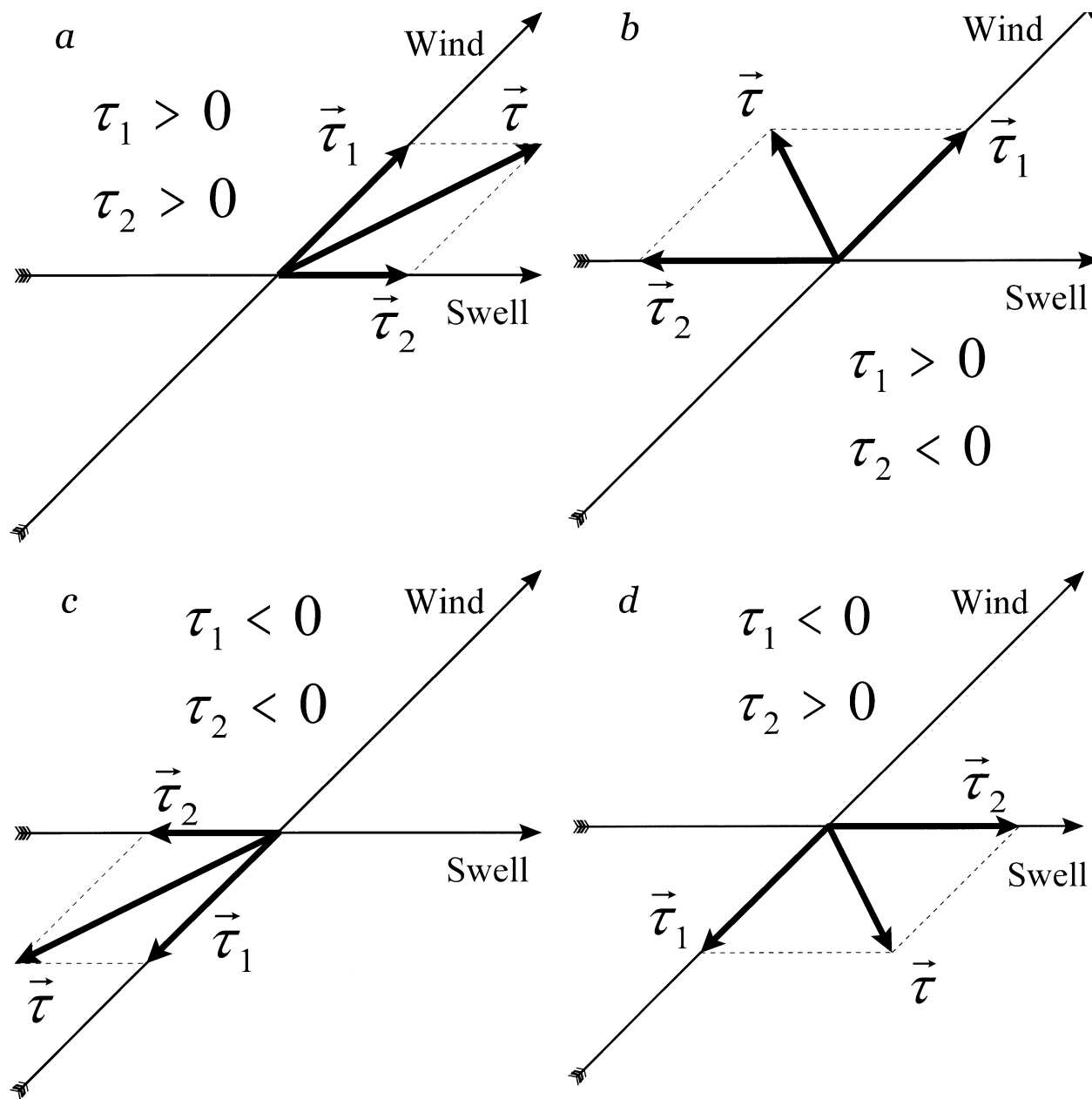
FIG. 2. Orientation of the total stress vector $\tau = \tau_1 + \tau_2$ in the case of mixed sea when swell is running obliquely in the wind direction, $\cos\theta_2 > 0$. Here τ_1 and τ_2 are defined by (6) and (7). Vector schemes in (a)–(d) are only schematics, and therefore the vectors are out of scale.

shown in Figs. 2 and 3 with the field data is given in section 4.

3. Three *FLIP* datasets

We use data collected by NOAA/ETL and WHOI during three campaigns aboard the R/P *FLIP*. Data were taken in the Pacific in September of 1993 during the San Clemente Ocean Probing Experiment (SCOPE), in April–May of 1995 during the Marine Boundary Layer II (MBL II) experiment, and in September of 1995 dur-

ing the Coastal Ocean Probing Experiment (COPE). Selection of the *FLIP* data is associated with the fact that a conventional ship is a less-ideal observation platform for this kind of study than a moored (or fixed) platform. Among other things, *FLIP* is more suited to multilevel turbulent and surface wave measurements and provides less distortion of air flow than a conventional ship.

The ETL–WHOI seagoing flux system was deployed aboard *FLIP*, and descriptions of the measuring system can be found in Fairall et al. (1997), Edson et al. (1998), and Hare and Fairall (1998). The data have been edited
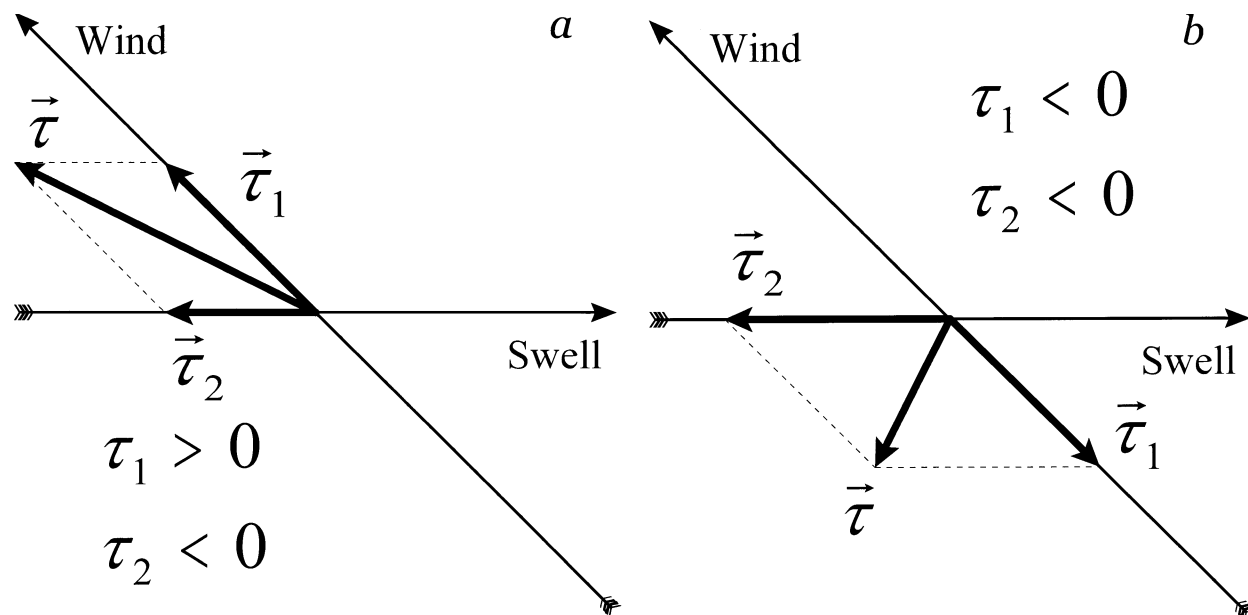
FIG. 3. Same as Fig. 2 but for the counterswell cases, $\cos\theta_2 < 0$.

for unfavorable relative wind directions, mean wind vector tilt, contamination of the turbulence data by the ship's wake, precipitation, and salt contamination. Based on the established criteria, the best flux estimate from the data has been used. The MBL II and COPE data have simultaneous wind and stress measurements at several levels, and the SCOPE data were taken at one level.

In the SCOPE experiment, the R/P *FLIP* was moored about 15 km northwest of San Clemente Island off of the southern California coast (33°N, 118°W). Measurements were taken from 17 to 29 September 1993. The entire SCOPE time series for wind speed, wind and swell direction, and air and sea temperature are shown in Fig. 4. Stress components and the stress direction direction are presented in Fig. 5. Winds were not strong, averaging about 4 m s^{-1}. Wind directions were predominantly from the northwest, but the influence of the mesoscale land–sea contrast caused some modulation on a diurnal cycle (apparent as oscillations in the wind and τ_x in Fig. 5). A northwest swell was moderate but almost always present, and the direction of the waves was very constant, about 300°, as shown in Fig. 4. Swell direction is based on the routine visual observations made by observers from the *FLIP* bridge. Data include 50-min-averaged observations of covariance and inertial-dissipation estimates of the turbulent fluxes of momentum, sensible and latent heat, mean meteorological variables, radiation fluxes, and the convective boundary layer height. The instruments were deployed at the end of an 18-m-long port boom, 11 m above the sea surface. Surface wave parameters were measured by an Air–Sea Interaction Array (ASIA) designed and constructed for SCOPE. Some other relevant information about the

SCOPE data, including a description of ASIA and wave conditions, can be found in papers by Fairall et al. (1996) and Grachev and Fairall (1997, 2001).

During the MBL II experiment, R/P *FLIP* was moored 50 km west of Monterey, California. A vertical instrumented mast was deployed from the end of the port boom, providing optimal exposure of the meteorological sensors for northwesterly winds. The mast extended from roughly 3 to 18 m above the sea surface and supported the sonic anemometers, cup anemometers, wind vanes, and the wave wire. To measure the velocity profile, a number of cup anemometers were deployed between 3.86 and 18.37 m above mean sea level. Several Gill Instruments, Ltd., Solent sonic anemometers were used for measuring the surface stress as well as wind speed and directions at several levels. In the current study, we use data obtained at three levels: 5.01, 8.98, and 14.03 m. These measurement heights differ approximately 1 m from the heights originally computed aboard *FLIP* (e.g., Wetzel 1996), because an adjustment was needed after the waves hit the bottom of the mast. Wave direction and height were also obtained from a nearby NOAA buoy. The general character of the dataset shows that a variety of conditions occurred (Fig. 6). During the first several days, the wind direction was southwest, turning gradually to northwest for yeardays (YD) 122–129. A low pressure system began to form over California at YD 122 and strengthened during the week. On the fifth day, the system began to weaken, and wind speed decreased without changing direction. The wind magnitude showed long periods of acceleration and deceleration, providing a steady buildup of the sea and a decaying sea between YD 123 and 125 and reaches a second maximum at YD 127. During this pe-
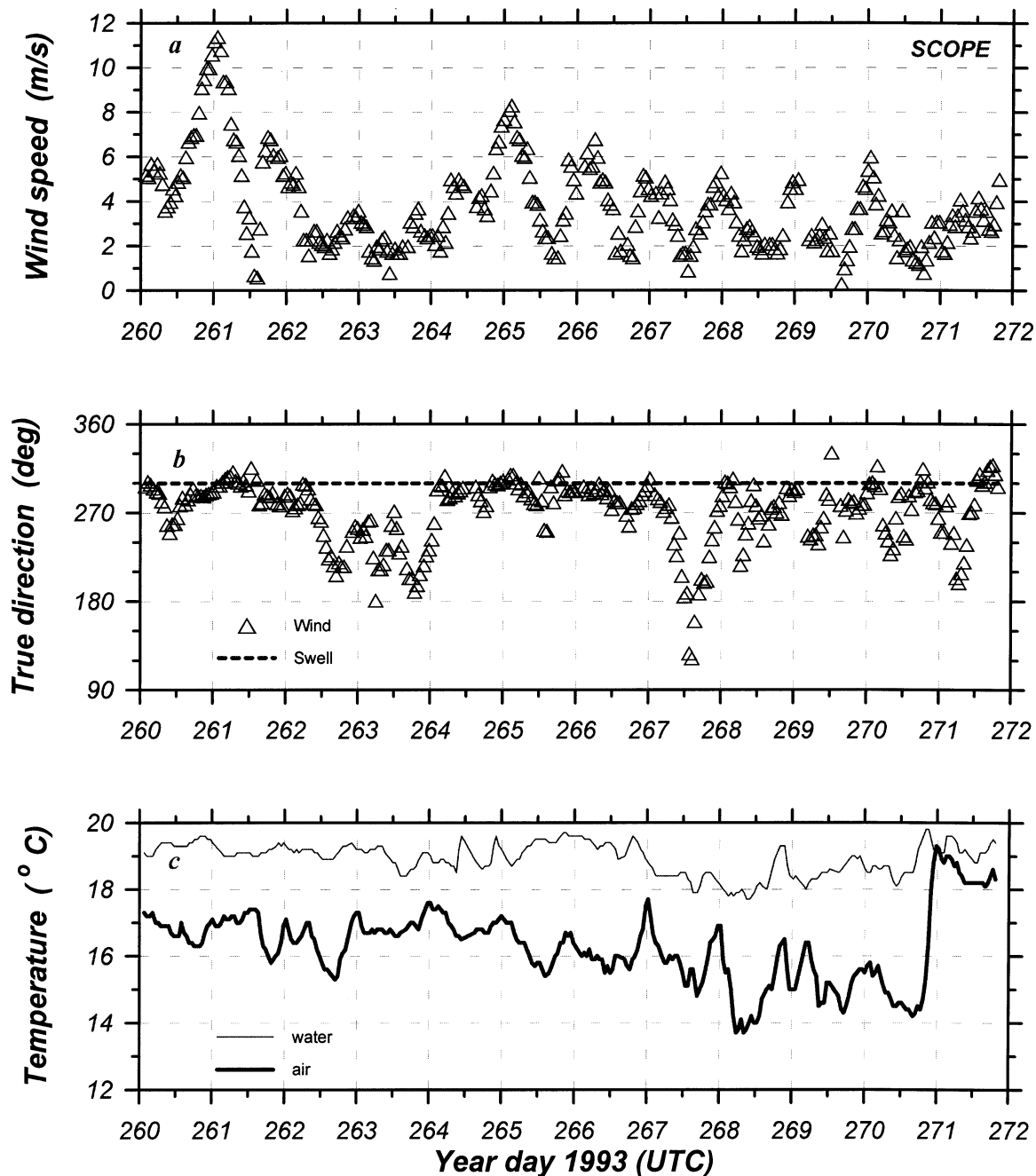
FIG. 4. Time series of (a) wind speed, (b) wind and swell direction, and (c) air (solid line) and sea (thin line) temperature during SCOPE.

riod, the mean winds reached velocities greater than 15 m s^{-1}, and the peak waves reached heights of 6 m. The lowest and second lowest cup anemometers were lost on YD 125. Note that during YD 123–128 the wind and swell directions were predominantly from the northwest, similar to the SCOPE observations (Fig. 6). These conditions are typical of those generally found off of the coast of California (cf. Fig. 4). In the earlier period (before YD 122), a lack of significant buildup of waves was observed, possibly because of an opposing swell

(280°) and wind (150°). Time series of the stress components and the stress direction at different levels are shown in Fig. 7. The turbulent statistics for the MBL II experiment used here were calculated based on the 1-h averaging time. Data with unfavorable relative wind directions (between 50° and 190°)—for example, during YD 121—have been rejected from the stress data analysis (Fig. 7). Some other details about MBL II, including description of the wave conditions, are given by Wetzel (1996), Miller et al. (1997), and Edson et al. (1998).
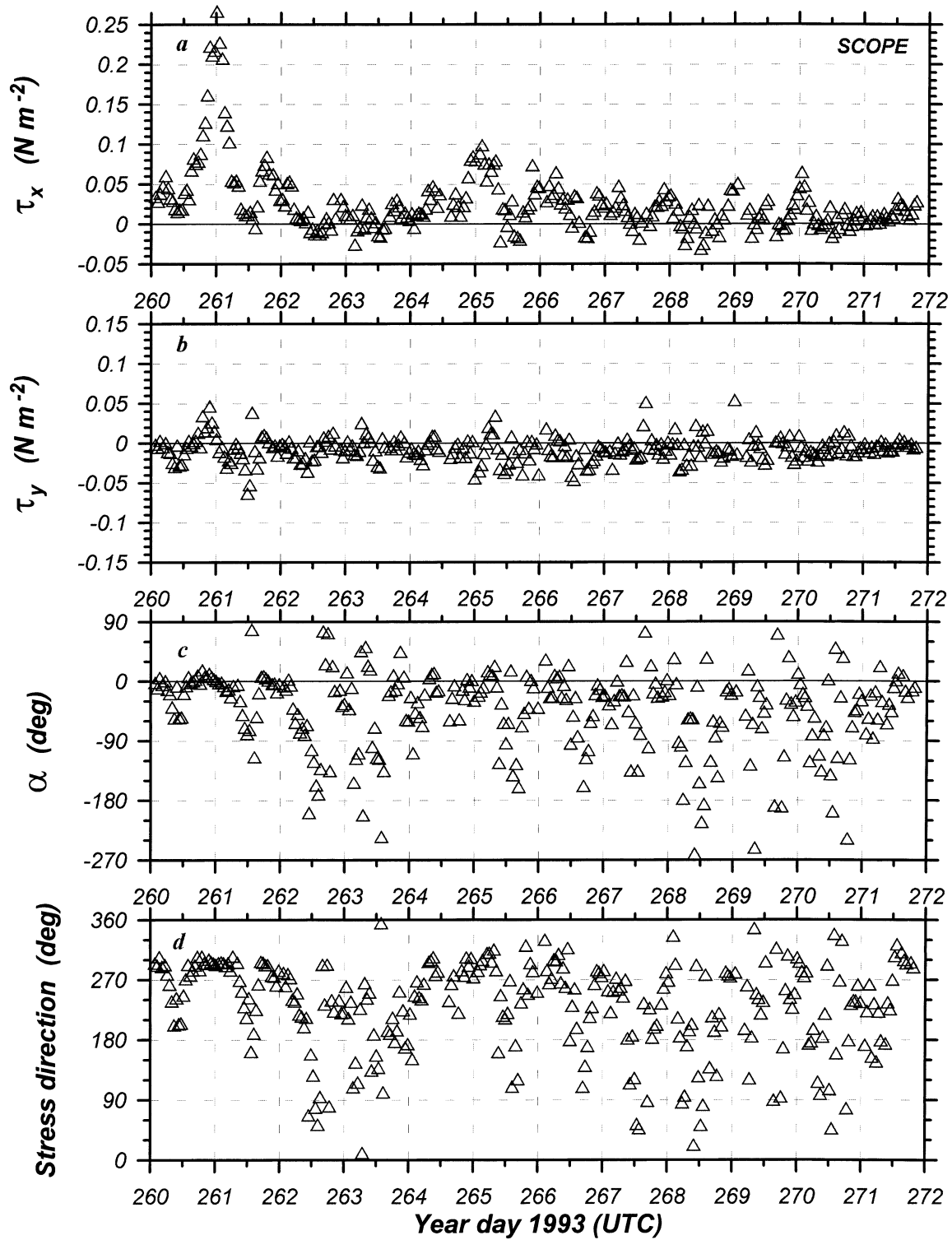
FIG. 5. Time series of (a) downwind stress component τ_x and (b) crosswind stress component τ_y, (c) stress offwind angle α, [see (3)], and (d) true stress direction during SCOPE. All angles are calculated using the meteorological convention: e.g., 270° means wind (or stress) is from the west and negative angles in (c) correspond to counterclockwise rotation.
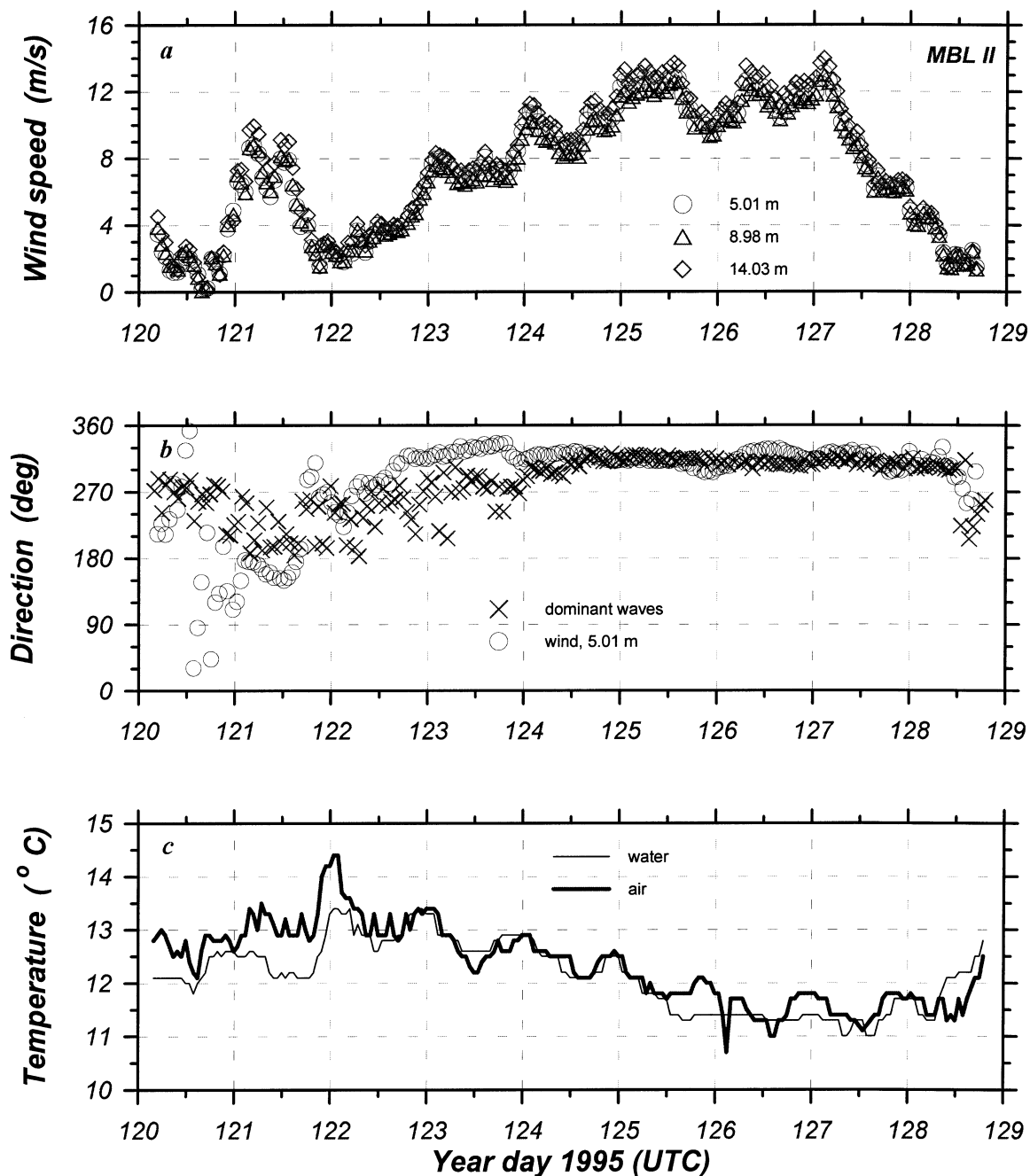
FIG. 6. Same as Fig. 4 but for the MBL II data. The (a) wind speed and (b) wind direction are derived from sonic anemometers. Different symbols correspond to different levels of sonic anemometers in (a). For clarity of presentation, only the wind direction from the 6.27-m level is presented in (b). (b) Wave direction and (c) air and sea temperature are obtained from the NOAA buoy.

In the COPE experiment, *FLIP* was moored at 150-m depth about 20 km off of the coast of northern Oregon just west of Tillamook (45°45.22′N, 124°16.9′W) on 10 September 1995. The location was chosen for the prevalence of tidally forced internal waves over a well-defined shelf break about 70 km offshore. The unusually shallow water for this mooring results from the requirement to be within range of the shore-based radars. Two

research vessels (R/P *FLIP* and R/V *Snowgoose*), several research aircraft (including a blimp), and a variety of shore-based remote sensing systems were involved (Kropfli and Clifford 1996; Fairall and Hare 1997; Hare and Fairall 1998). Most of the measurements were online by 18 September (YD 261). Conditions during COPE were variable, with winds from 0 to 17 m s^{-1} and heavy swells traveling most of time crosswind (Fig.
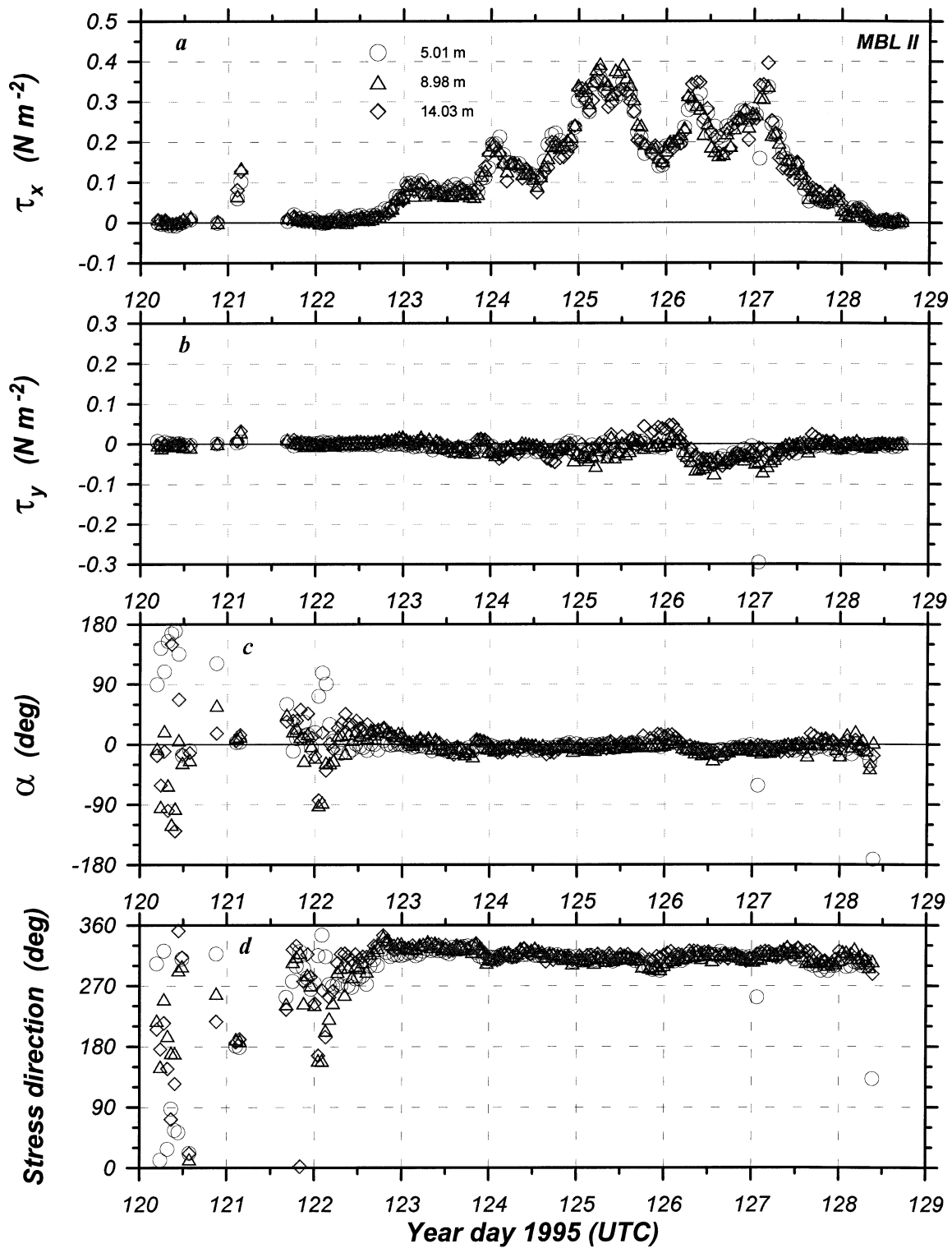
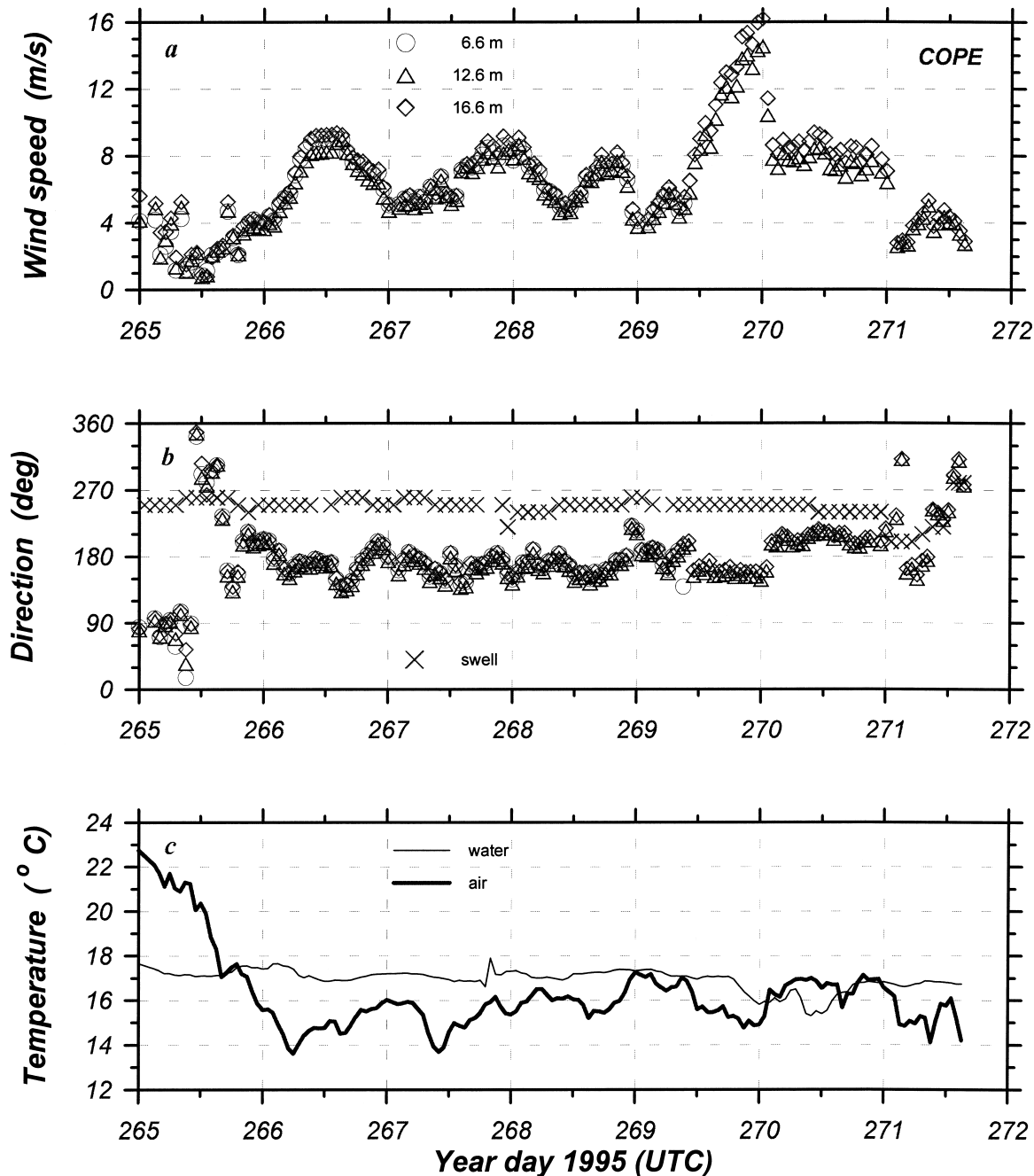FIG. 7. Same as Fig. 5 but for the MBL II data. Nomenclature is the same as in Fig. 6a.

FIG. 8. Same as Fig. 4 but for the COPE data. Different symbols correspond to the three levels of sonic anemometers.

8). Surface signatures of internal wave packets were observed almost daily (Kropfli et al. 1999; Ostrovsky et al. 1999; Otto et al. 1998). There were almost continuous problems with unfavorable environmental factors. Two days of strong easterly winds led to a plague of insects and strong wakes from *FLIP* onto the turbulent flux instruments. For this reason, turbulent data before the middle of 22 September (YD 265) have been rejected from the analyses (Fig. 9). During the period of 22–28 September (YD 265–271), wind directions

were predominantly from the south and the direction of the swell was constant, about 250°–260°, with periods of 14–15 s. Swell direction and period are derived from visual observations from the *FLIP* bridge and analyses of the Doppler radar images obtained from a nearby hillside about 4 km from the shore and 744 m above sea level (Ostrovsky et al. 1999). An unusually strong storm with 17 m s^{-1} winds struck *FLIP* on 26 September (YD 269). An unprecedented dataset on turbulence, internal waves, and ocean surface properties was obtained.
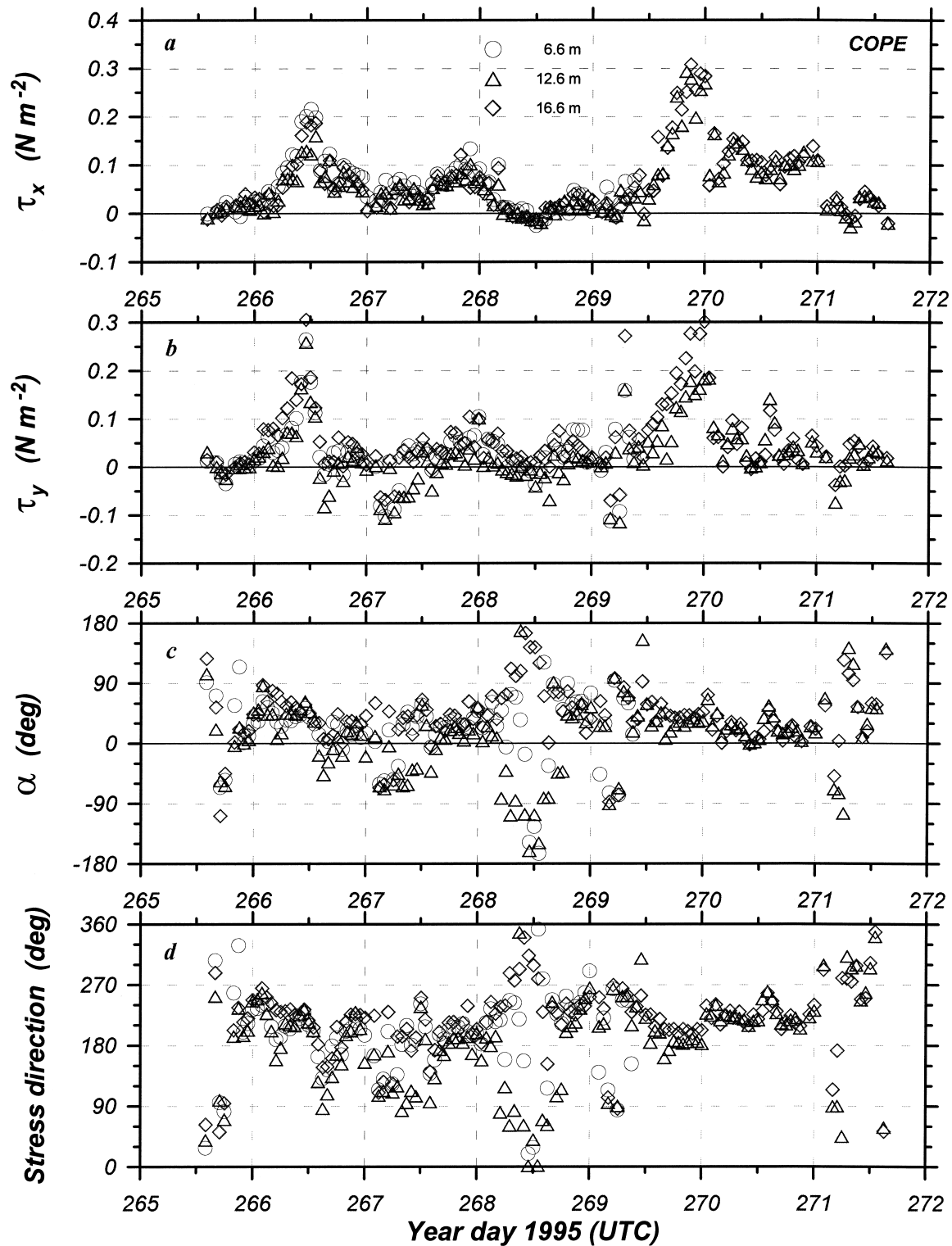
FIG. 9. Same as Fig. 5 but for the COPE data. Nomenclature is the same as in Fig. 8a.

Three sonic anemometers were mounted on the 20-m vertical mast at 6.6, 12.6, and 16.6 m above the sea. This mast was deployed from a port-side boom, and it was located 20 m away from R/P *FLIP* in a nearly zero flow-distortion region. The processed fluxes represent 1-h averaged data.

A time series of the stress components show that the crosswind stress component τ_y generally is insignificant with respect to the alongwind stress component τ_x for SCOPE (Fig. 5) and MBL II (Fig. 7) data. Only during light winds is the magnitude of τ_y comparable to τ_x. In contrast, during COPE, the magnitude of τ_y is the same order as τ_x even for strong winds (Fig. 9). This is because SCOPE and MBL II are generally characterized by conditions in which the swell was running in the same direction as the wind or a swell–wind angle was small (Figs. 4 and 6). During COPE, heavy swells traveling most of the time approximately crosswind (Fig. 8) caused high values of crosswind (vw) covariance. This is clear evidence that waves propagating at an oblique direction with respect to wind direction may cause nonzero crosswind covariance that results in deviation of the stress vector from even a strong mean wind flow.

4. Directional analysis of the wind stress

In this section we use data collected during the three *FLIP* expeditions to examine the behavior of the stress direction and verify the approach derived in section 2. Figures 5, 7, and 9 show the time series of the stress components τ_x, τ_y, the relative angle α between stress and wind direction [see (3)], and the true stress angle for the SCOPE, MBL II, and COPE data, respectively. Data obtained during the three *FLIP* campaigns cover a wide range of the wind and wave conditions being mutually complementary, and therefore the direction of the stress vector in Figs. 5, 7, and 9 varies over a wide range. The range of the stress directions varies from cases in which the stress direction coincides with the wind direction to cases in which the stress is directed across or even opposite to the wind.

Our approach is based on the idea that the stress direction is basically governed by both wind and swell directions (direction of wind waves is frequently close to the wind direction). For this reason we split the stress vector in two vectors aligned with wind ($\boldsymbol{\tau}_1$) and swell, ($\boldsymbol{\tau}_2$), respectively, in (6) and (7). Now we examine the behavior of τ_1 and τ_2 in detail. Figure 10 presents τ_1 and τ_2 stress components plotted against mean wind speed (counterswell data are not included). The transformation from the rectangular Cartesian reference frame associated with the direct measured τ_x and τ_y to the nonrectangular reference frame associated with τ_1 and τ_2 is described by (7). As mentioned in section 2, this transformation is impossible for $\sin\theta_2 = 0$, because for $\sin\theta_2 \rightarrow 0$, τ_1 and $\tau_2 \rightarrow \pm\infty$ [see (7)]. To avoid this problem, we consider data only with $|\sin\theta_2| > 0.2$.

Thus in Fig. 10 (and further in Figs. 11–13), we discard data if the swell travels at angles less than $\pm 12°$ with respect to the wind (in the same direction and direction opposite to the wind). Because our approach is derived for stress on the sea surface, $z = \eta$, it makes sense to plot height-averaged stress data in the case of the multilevel measurements (MBL II and COPE data). It also reduces the data scatter. Values of τ_1 and τ_2 for MBL II and COPE presented here are derived from τ_x and τ_y [see (7)], which have been averaged over three levels of measurements.

Figure 10 shows that both τ_1 and τ_2 decrease monotonically with decreasing wind speed. However, on the average, τ_1 approaches zero for $U \lesssim 2$ m s^{-1}, whereas τ_2 reaches zero and reverses sign in light winds, $U \lesssim 4$ m s^{-1}. According to section 2, τ_1 is a sum of the positive shear stress and wave-induced stress due to pure wind waves. Both parts of τ_1 are associated with a local wind field, and, therefore, they generally tend to zero as the wind speed approaches zero. Negative values of τ_1 in Fig. 10a may be associated with a decaying sea state as discussed in section 2. Swell is not associated with a local wind field, and it does not necessarily dissipate in calm weather. For this reason τ_2 does not approach zero at $U \rightarrow 0$. In the regime with swell traveling faster than the local wind in the same direction, waves will accelerate airflow above, and, therefore, $\tau_2 < 0$. Figure 10 shows that, on average, τ_2 reaches zero around wind speed $U \approx 5$–6 m s^{-1}, which corresponds to wave age $c_{p2}/U \approx 3$ (this follows from similar plots of τ_2 vs wave age). According to (7) and data from Fig. 10, the alongwind stress component τ_x will decrease monotonically with decreasing wind speed, reach zero, and reverse sign to negative similar to τ_2 (Fig. 10a). However, the sign reversal of τ_x will occur at a wind speed less than in the τ_2 case (Fig. 10b) because τ_x is a sum of positive and negative terms in light winds [cf. (7) and Fig. 10]. This is consistent with results obtained earlier by Grachev and Fairall (2001). They found that τ_x reverses sign around a wind speed of $U \approx 1.5$–2 m s^{-1} (wave age $c_{p2}/U \approx 10$). For high winds, $U \gtrsim 8$ m s^{-1}, the values of τ_1 and τ_2 are comparable (Fig. 10), and the contribution to the total stress associated with the swell is comparable to the wind contribution. Note that, for fixed wind speed, τ_2 may also depend on swell amplitude.

To investigate the stress direction issue further, we divide the data into several groups based on the behavior of τ_1 and τ_2 shown in Fig. 10 on the wind speed and direction of the wind relative to the dominant wave direction. Consider a case of moderate and strong winds, $U \gtrsim 5$–6 m s^{-1} ($c_{p2}/U \lesssim 3$), blowing in the direction of the swell propagation, $\cos\theta_2 > 0$. According to Figs. 5, 7, and 9, the mean stress direction is generally in line with the wind and dominant wave direction provided the wind and waves are approximately aligned ($\cos\theta_2 \approx 1$). For this reason, most of the SCOPE data associated with high winds do not appear in Fig. 10. This
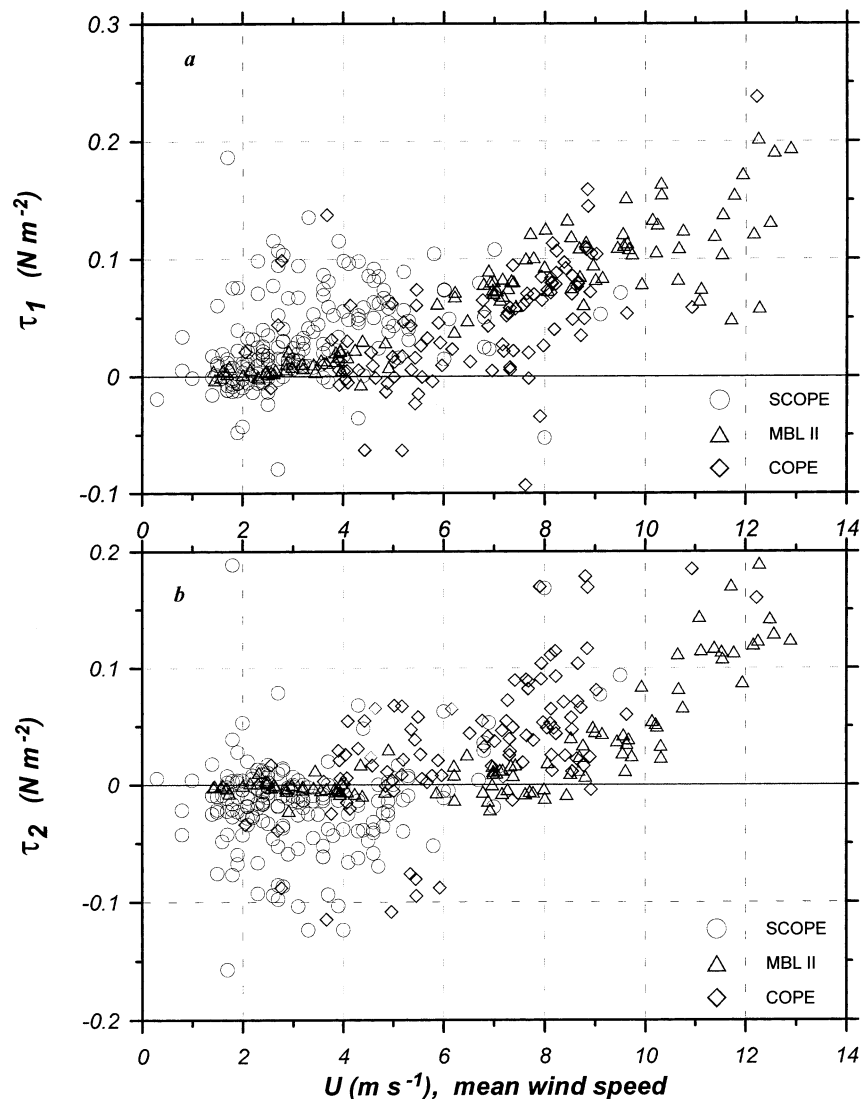
FIG. 10. Stress components τ_1 and τ_2 vs mean wind speed ($\cos\theta_2 > 0$). Values of τ_1 and τ_2 are derived from (7) based on τ_x and τ_y data. Different symbols correspond to data obtained during different cruises. Values of τ_1 and τ_2 for MBL II and COPE data are height average.

situation was observed during the moderate and strong wind events in SCOPE and for most of the time during MBL II. In this case, the stress off-wind angle $\alpha \approx 0°$ (Figs. 5c and 7c). However, MBL II data for high winds provide an example in which $\alpha \neq 0°$. During YD 125.5–127, the wind changed direction relative to the dominant waves (Fig. 6b), which led to a change of the sign of τ_y (Fig. 7b). For example, the YD-126 wind is directed to the left of the dominant waves (wind direction is 297°; wave direction is 310°), and $\tau_y > 0$. For YD 126.5, the wind is directed to the right of the dominant waves (wind direction is 329°; wave direction is 309°), and $\tau_y < 0$. In both cases, the stress vector deviates to the wave direction (see sign convention for τ_y in section 1). One may expect that this is due to the influence of waves on stress direction. Note the high correlation of mea-

sured τ_y for all three levels in MBL II (Fig. 7b). During COPE the wind often blew obliquely to the swell direction (Fig. 8b). Large angles between the wind and swell (swells travel approximately crosswind) cause high values of the crosswind component with the same sign (Fig. 9b). As a result, the stress off-wind angle (3) deviates substantially from zero, and $\alpha \approx 30°$ even for high winds (Fig. 9c). Comparison of Figs. 8b and 9d shows that with the exception of light-wind and counterswell events, the stress vector over YD 266–271 (23–28 September) generally lies between wind direction (about 180°) and swell direction (about 260°). Figure 11 shows the decomposition of the wind stress in the reference frame associated with the wind and swell direction (i.e., τ_1 vs τ_2 coordinates). According to our approach, the stress vector lies in an acute angle between
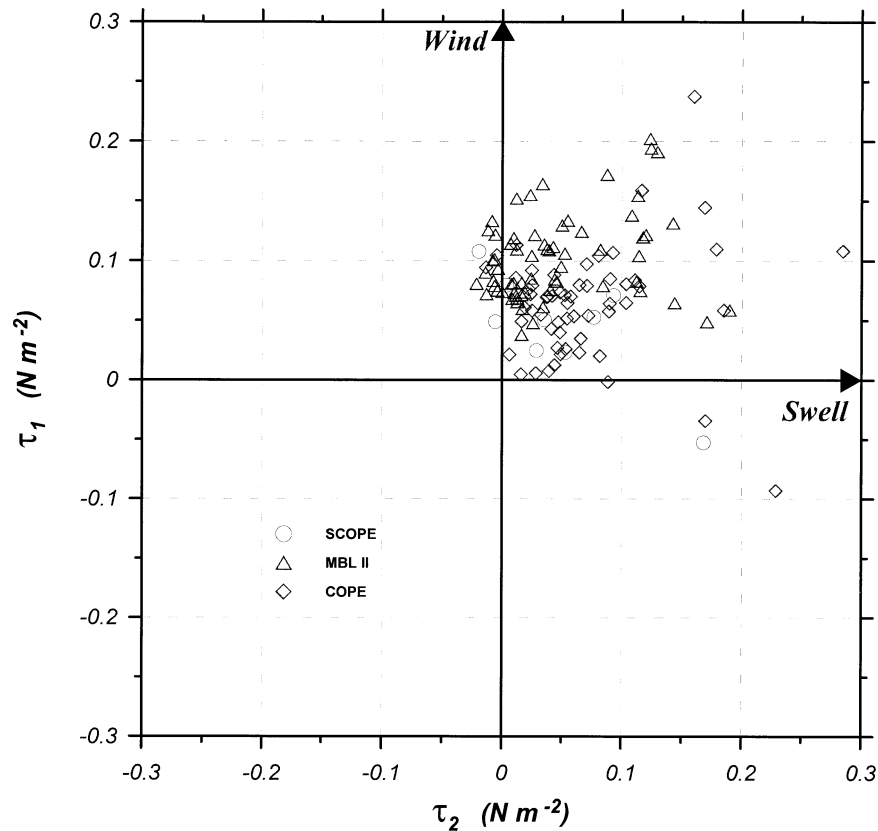
FIG. 11. Decomposition of the stress vector in the wind–swell coordinate system (i.e., τ_1 vs τ_2 coordinates) for the case in which swell propagates in the wind direction ($\cos\theta_2 > 0$) and there are moderate and strong winds ($U > 6$ m s^{-1}). Vector diagrams for this case are shown in Figs. 1 and 2a. Nomenclature is the same as in Fig. 10.

the wind direction and the wave direction and is facing the wind–wave direction, that is, $\tau_1 > 0$ and $\tau_2 > 0$ (see Figs. 1 and 2a). Values from all three *FLIP* datasets presented in Fig. 11 satisfy the following criteria: $\cos\theta_2 > 0$, $|\sin\theta_2| > 0.2$, and $U > 6$ m s^{-1}. Points in Fig. 11 are clustered more in the upper-right quadrant, $\tau_1 > 0$ and $\tau_2 > 0$. The stress vector has a direction that is, in general, a blend between the wind direction and the swell direction. This result agrees with previous studies such as Geernaert et al. (1993), Rieder et al. (1994, 1996).

High values of α (Figs. 5, 7, and 9) are generally associated with light-wind events. As the wind speed decreases (c_{p2}/U increases), the swell-induced stress τ_2 decreases, reaches zero, and reverses sign (see section 2). As a result, the stress vector deviates significantly from the wind and swell directions, including cases in which the stress is directed across ($\tau_x = 0$ and $\tau_y \neq 0$) or even opposite to the wind ($\tau_x < 0$ and $\tau_y = 0$). Examples of these situations can be found in Figs. 5, 7, and 9. For conditions observed during SCOPE, Grachev and Fairall (2001, Fig. 5) showed that, as wind speed decreases, the stress vector turns in a counterclockwise direction at about 180°, from the wind–swell

direction in high winds, through the crosswind direction, to nearly opposite the wind and swell direction. The regime in which the surface stress is aligned opposite the wind direction corresponds to upward momentum transfer (Grachev and Fairall 2001). This regime is observed in SCOPE during YD = 262.5, 265.6, and 268.5 (Fig. 5), in MBL II during YD 120.4 (Fig. 7), and in COPE during YD 268.5 (Fig. 9). Note that the upward momentum flux in COPE is caused by wind waves during decaying wind events, because the swell is nearly perpendicular to the wind. A sign reversal occurs at $U \approx 4$ m s^{-1} (Fig. 8a), which is consistent with the results of Drennan et al. (1999) obtained in Lake Ontario, and is higher than the $U \approx 2$ m s^{-1} obtained by Grachev and Fairall (2001) for the ocean swell regime. This variation may be associated with higher slopes of wind waves as compared with ocean swells. Note that for COPE YD 268.5 (Fig. 9c), the stress vector turns about 180°, and finally it is nearly opposite to the wind (upward momentum transfer) and perpendicular to the swell. It is particularly remarkable that the stress vector turns in different directions at different levels. Thus, in this case, τ_2 reverses sign with height, and this issue will be discussed later.
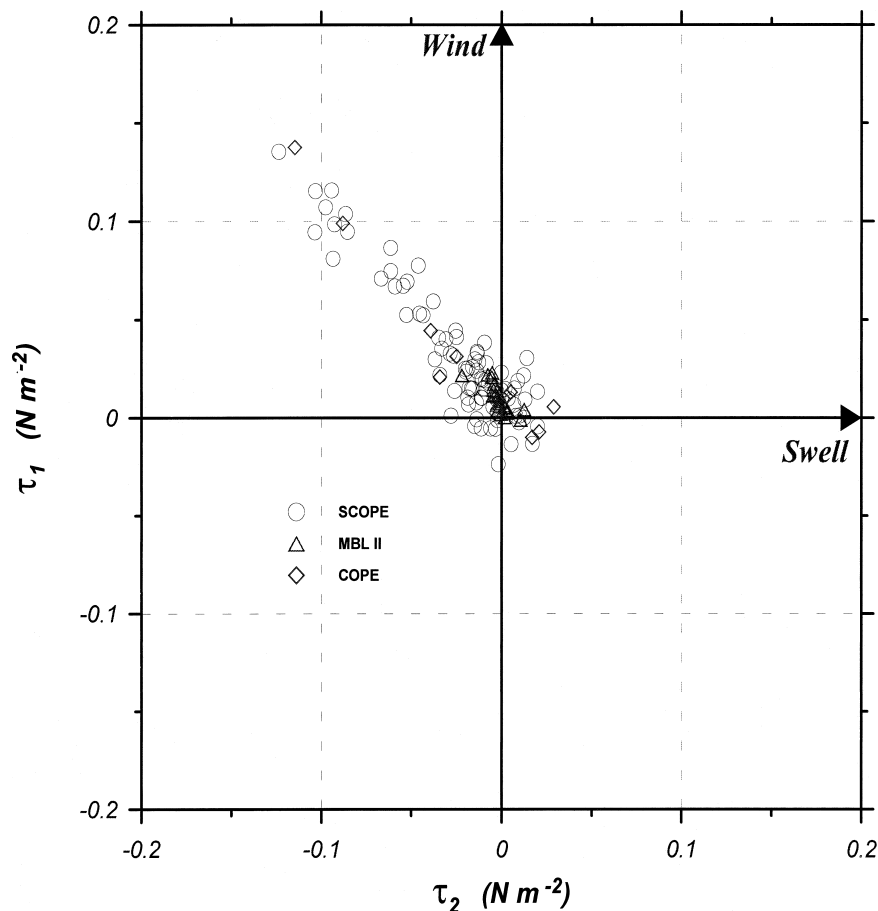
FIG. 12. Same as Fig. 11 but for the case in which swell propagates in the wind direction ($\cos\theta_2 > 0$) and light winds exist (2 m s$^{-1} < U < 6$ m s^{-1}). Vector diagram for this case is shown in Fig. 2b.

In the case in which $\tau_2 < 0$ with τ_1 still positive, the stress vector lies at an obtuse angle between the wind direction and the opposite wave direction, and it is facing the direction that is opposite to the direction of wave propagation (Fig. 2b). This situation is usually associated with winds $2 \lesssim U \lesssim 4$–6 m s^{-1} and background swell. This case was described by Grachev and Fairall (2001), where they showed that a deviation of the stress vector direction from the wind vector direction during light winds is not random, and it is governed by both the swell direction and the wind direction (their Fig. 5). Figure 12 shows a decomposition of the wind stress for this regime at the $\boldsymbol{\tau}_1$ versus $\boldsymbol{\tau}_2$ coordinates (relative to wind and swell directions). Most of the points are grouped in the upper-left quadrant, $\tau_1 > 0$ and $\tau_2 < 0$, as predicted in section 2. The cluster of points is stretched along the bisector. This is associated with self-correlation in the τ_1 and τ_2 solutions in (7), when τ_y is significant when compared with τ_x, and $|\theta_2|$ is small. However, this fact does not affect our approach, because self-correlation can change the relative positions of the

points inside the quadrant but cannot change the quadrant itself; that is, the signs of τ_1 and τ_2.

Note that high values of α are not observed exclusively in the case of light winds. Figure 9c shows examples of high values of α (up to $60°$) for high winds during COPE. For example during YD = 269.5–271, high values of α are observed for $U = 7$–16 m s^{-1} and $\cos\theta_2 > 0$. Another example at YD ≈ 266.6 ($U \approx 9$ m s^{-1}) is associated with a situation in which the wind blows against the swell ($\cos\theta_2 < 0$). In this situation, $\tau_2 < 0$ (counterswell regime) and $\tau_1 > 0$ (high wind), and the appropriate vector diagram is shown in Fig. 3a. A projection of the stress vector on the wind direction τ_x is positive in this case [see the first equation in (7)], and a projection of the stress vector on the swell direction, $\tau_\theta = \tau_1 \cos\theta_2 + \tau_2$, is always negative. The counterswell regime for the SCOPE data was considered by Grachev and Fairall (2001). They showed that in this regime, $\tau_x > 0$ and $\tau_\theta < 0$ [see Grachev and Fairall's (2001) Figs. 4 and 6, respectively]. Plots of τ_1 vs τ_2 for the counterswell cases are shown in Fig. 13. Although
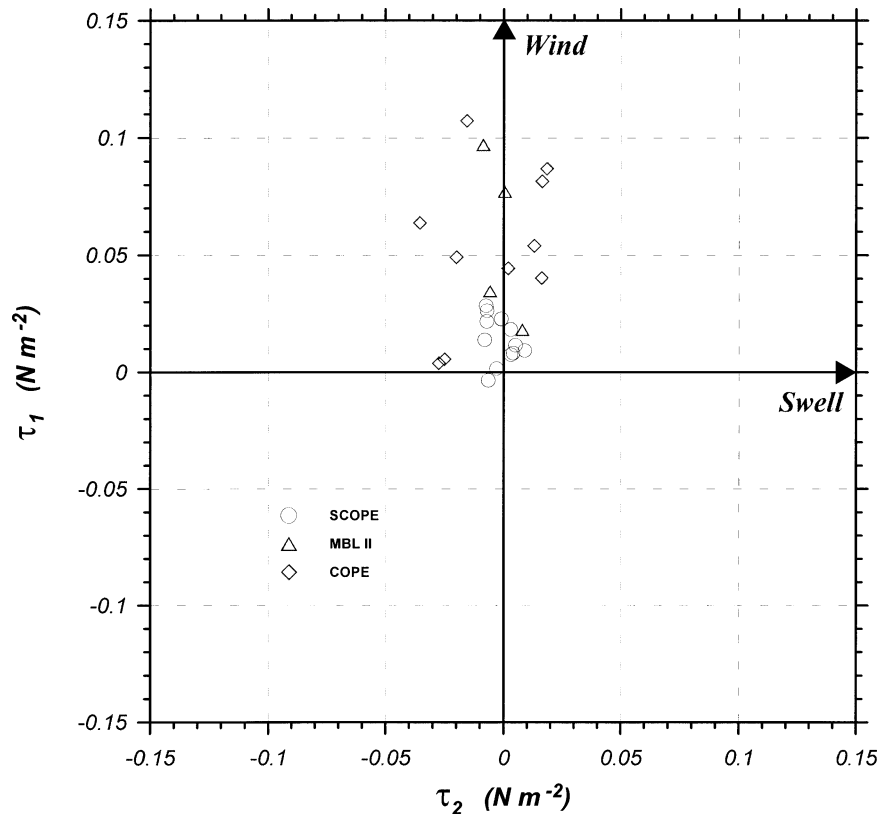
FIG. 13. Same as Fig. 11 but for the counterswell cases ($\cos\theta_2 < 0$). Vector diagram for this case is shown in Fig. 3a.

most of the points are clustered in the quadrant with $\tau_1 > 0$ and $\tau_2 < 0$ as predicted above, the scatter of data is larger than in Figs. 11 and 12. Some points in Fig. 13 are associated with the "prohibited" values $\tau_2 > 0$. We consider here only three cases of the six situations shown in Figs. 2 and 3. These cases are most common and statistically more representative, whereas consideration of the cases shown in Figs. 2c, 2d, and 3b requires more experimental points.

5. Discussion

Figures 10–13 show large scatter of the stress components and directions, including cases in which τ_1 and τ_2 have "wrong" signs—for example, $\tau_2 > 0$ in Fig. 13. We discuss here some possible sources responsible for the scatter. First, some other factors neglected in our analysis can affect the surface stress. For example, internal waves and surface currents (e.g., Cornillon and Park 2001) and the structure of the boundary layer as controlled by large-scale atmospheric eddies could have an influence on τ (e.g., Geernaert 1996). Temporal nonstationarity adds a level of complexity that is not included in the current approach. Rieder (1997) reported a temporal lag of $O(4)$ h between the peak in wind speed and the peak in the drag coefficient (5). In a similar way, different turning rates for the wind direction and direction of the wind waves

[e.g., see nonstationary events in Rieder et al. (1996), their Fig. 2] and therefore between the wind and wind stress vectors (Quanduo and Komen 1993) may also contribute to the scatter of τ_1 and τ_2.

Another possible reason for the scatter is associated with the measurement procedure and accuracy. The main uncertainty is associated with the estimation of the swell direction. It seems likely that uncertainty of the swell direction based on visual observations from a ship is as much as 20° for individual estimates, which leads to errors in the determination of the angle θ_2. However, an approximately constant swell direction during SCOPE and COPE reduces the individual measurement error, and the criterion $|\theta_2| < 12°$ reduces the scatter. Stress estimates derived from a sonic anemometer are sensitive to the tilt of the anemometer (Wilczak et al. 2001). Small errors in the alignment of the anemometer can cause large errors in the measured stress components because of cross-contamination of velocities, wherein the longitudinal component of the wind vector appears as vertical velocity and vice versa. The most commonly used method, applied in the current study, is associated with a double rotation of the anemometer coordinate system. Rotation is needed to place the anemometer in the streamwise coordinate system. The first rotation sets $\langle v \rangle = 0$, and the second rotation sets $\langle w \rangle = 0$. However,

the double rotation scheme does not correct for lateral tilt, and, for this reason, mean biases may occur in cross-stream stress and, therefore, in α. This effect may be responsible for behavior of the the stress vector at different heights observed in COPE YD 268.5 and discussed in the previous section. According to Wilczak et al. (2001), for a physical tilt of the anemometer or a terrain-induced tilt of the flow, these errors can be of the same order as the true stress and depend on its initial orientation. For this reason, in Figs. 10–13, we use height-averaged stress components to reduce the data scatter.

The approach derived in section 2 is based on the idea that the direction of the local wind waves coincides with the wind direction (vector $\boldsymbol{\tau}_{\mathrm{wave1}}$ is codirectional with the wind vector). This hypothesis simplifies the real situation. In some situations, wind waves can propagate at oblique angles to the wind. Because this effect is not considered in section 2, it may cause additional scatter of points in Figs. 10–13. However, our approach allows us to describe this situation based on the more general (11) instead of (12). In this case, the wind stress direction is governed by the wind direction, direction of the swell, and the wind-wave propagation direction. The direction of the wind waves, as well as the swell direction, can be derived from the wave directional spectra. Note that a more accurate stress directional analysis should be accompanied by an analysis of the directional spectrum of surface elevation (e.g., Donelan et al. 1997) and the directional wave-breaking statistics.

6. Conclusions

In this study, the directional characteristics of the wind stress in different wind–wave regimes are considered. Based on the approach derived in section 2, the surface stress is a vector sum of the 1) pure shear stress (turbulent and viscous) aligned with the mean wind shear, 2) wind-wave-induced stress aligned with the direction of the pure wind-sea waves, and 3) swell-induced stress aligned with the swell direction (cf. Remy and Giovanangeli 1999). Because the direction of wind waves is frequently close to the wind direction, we split the stress vector into two vectors aligned with the wind $\boldsymbol{\tau}_1$ and swell $\boldsymbol{\tau}_2$ directions, respectively, as seen in (6) and (7). It is crucial for this study that the direction of the wind-wave-induced stress and the swell-induced stress components approximately (but not exactly) coincide with, or be opposite to, the direction of wave propagation (pure wind waves and swell, respectively). As a result the stress vector may deviate significantly from the mean wind flow, including cases in which the stress is directed across or even opposite to the wind. All possible situations associated with the stress-vector orientation are shown in Figs. 2 and 3.

Data obtained during the three field campaigns aboard the R/P *FLIP* are used to verify our approach. We consider three cases, two associated with the swell running

approximately in the wind direction, and one for a counterswell event. For moderate and strong winds, $U \gtrsim 5$–6 m s^{-1} ($c_{p2}/U \lesssim 3$), blowing in the direction of the swell propagation, it was found that the wind stress direction lies between the mean wind and the swell, $\tau_1 > 0$ and $\tau_2 > 0$ (cf. Geernaert et al. 1993; Rieder et al. 1994, 1996). This situation is shown in Figs. 1, 2a, and 11. In the case of $2 \lesssim U \lesssim 4$–6 m s^{-1} with background swell, the stress vector lies at an obtuse angle between the wind direction and the opposite wave direction, $\tau_1 > 0$ and $\tau_2 < 0$ (Figs. 2b, 12). This case is also discussed by Grachev and Fairall (2001). In the counterswell case with strong winds, the stress vector lies at an obtuse angle between the wind direction and the opposite wave direction, $\tau_1 > 0$ and $\tau_2 < 0$ (Figs. 3a, 13). Although the signs of τ_1 and τ_2 are the same as in Figs. 2b and 15, in the counterswell case, $\cos\theta_2 < 0$.

It is generally believed that the WBL depth is typically only one to two wave heights $[O(1 \text{ m})]$ in the wind-sea conditions, and a measurement level of order 10 m is well beyond the WBL. However according to the COPE data, high values of α are observed at all measurement levels, 6.6–16.6 m (see section 4). It is likely that, for the swell conditions discussed here, the WBL is much higher than $O(1 \text{ m})$ and extends beyond the measurement height even for high winds (up to 16 m s^{-1}).

The determination of the wind stress vector is important in many applications, especially those related to radar remote sensing of the ocean surface. Airborne and spaceborne scatterometers may detect the surface stress direction rather than the mean wind direction (Colton et al. 1995; Rufenach et al. 1998; Cornillon and Park 2001).

REFERENCES

Belcher, S. E., and J. C. R. Hunt, 1998: Turbulent flow over hills and waves. *Ann. Rev. Fluid Mech.,* **30,** 507–538.

Colton, M. C., W. J. Plant, W. C. Keller, and G. L. Geernaert, 1995: Tower-based measurements of normalized cross section from Lake Ontario: Evidence of wind stress dependence. *J. Geophys. Res.,* **100** (C5), 8791–8813.

Cornillon, P., and K.-A. Park, 2001: Warm core ring velocities inferred from NSCAT. *Geophys. Res. Lett.,* **28,** 575–578.

Donelan, M. A., 1990: Air–sea interaction. *The Sea,* B. LeMehaute and D. M. Hanes, Eds., Ocean Engineering Science, Vol. 9, John Wiley and Sons, 239–292.

——, and F. W. Dobson, 2001: The influence of swell on the drag. *Wind Stress Over the Ocean,* I. S. F. Jones and Y. Toba, Eds., Cambridge University Press, 181–189.

——, W. M. Drennan, and K. B. Katsaros, 1997: The air–sea momentum flux in conditions of wind sea and swell. *J. Phys. Oceanogr.,* **27,** 2087–2099.

Drennan, W. M., K. K. Kahma, and M. A. Donelan, 1999: On momentum flux and velocity spectra over waves. *Bound.-Layer Meteor.,* **92,** 489–515.

Edson, J. B., A. A. Hinton, K. E. Prada, J. E. Hare, and C. W. Fairall, 1998: Direct covariance flux estimates from mobile platforms at sea. *J. Atmos. Oceanic Technol.,* **15,** 547–562.

Fairall, C. W., and J. E. Hare, 1997: Bulk meteorological and turbulent flux measurements from R/V *Snowgoose* during the Coastal Ocean Probing Experiment. NOAA Tech. Memo. ERL ETL-279, Boulder, Colorado, 63 pp. [Available from the National Technical Information Service, 5285 Port Royal Rd., Springfield, VA 22161.]

——, A. A. Grachev, A. J. Bedard, and R. T. Nishiyama, 1996: Wind, wave, stress, and surface roughness relationships from turbulence measurements made on R/P *FLIP* in the SCOPE experiment. NOAA Tech. Memo. ERL ETL-268, Boulder, Colorado, 37 pp. [Available from the National Technical Information Service, 5285 Port Royal Rd., Springfield, VA 22061.]

——, A. B. White, J. B. Edson, and J. E. Hare, 1997: Integrated shipboard measurements of the marine boundary layer. *J. Atmos. Oceanic Technol.,* **14,** 338–359.

Friehe, C. A., J. A. Smith, K. F. Rieder, N. E. Huang, J.-P. Giovanangeli, and G. L. Geernaert, 2001: Wind, stress and wave directions. *Wind Stress over the Ocean,* I. S. F. Jones and Y. Toba, Eds., Cambridge University Press, 232–241.

Geernaert, G. L., 1988: Measurements of the angle between the wind vector and wind stress vector in the surface layer over the North Sea. *J. Geophys. Res.,* **93** (C7), 8215–8220.

——, 1990: Bulk parameterization for the wind stress and heat fluxes. *Surface Waves and Fluxes: Theory and Remote Sensing,* G. L. Geernaert and W. L. Plant, Eds., Vol. 1, Kluwer Academic, 91–172.

——, 1996: On modeling the wind stress direction based on thermal advection and surface waves. *The Air–Sea Interface, Radio and Acoustic Sounding, Turbulence and Wave Dynamics,* M. A. Donelan, W. H. Hui, and W. J. Plant, Eds., RSMAS, University of Miami, 421–427.

——, F. Hansen, M. Courtney, and T. Herbers, 1993: Directional attributes of the ocean surface wind stress vector. *J. Geophys. Res.,* **98** (C9), 16 571–16 582.

Grachev, A. A., and C. W. Fairall, 1997: Dependence of the Monin–Obukhov stability parameter on the bulk Richardson number over the ocean. *J. Appl. Meteor.,* **36,** 406–414.

——, and ——, 2001: Upward momentum transfer in the marine boundary layer. *J. Phys. Oceanogr.,* **31,** 1698–1711.

Hare, J. E., and C. W. Fairall, 1998: Bulk meteorological and turbulent flux measurements from R/P *FLIP* during the Coastal Ocean Probing Experiment. NOAA Tech. Memo. ERL ETL-288, Boulder, Colorado, 158 pp. [Available from the National Technical Information Service, 5285 Port Royal Rd., Springfield, VA 22061.]

——, T. Hara, J. B. Edson, and J. M. Wilczak, 1997: A similarity analysis of the structure of airflow over surface waves. *J. Phys. Oceanogr.,* **27,** 1018–1037.

Hsu, C.-T., and E. Y. Hsu, 1983: On the structure of turbulent flow over a progressive water wave: Theory and experiment in a transformed wave-following coordinate system. Part 2. *J. Fluid Mech.,* **131,** 123–153.

——, ——, and R. L. Street, 1981: On the structure of turbulent flow over a progressive water wave: Theory and experiment in a transformed, wave-following coordinate system. *J. Fluid Mech.,* **105,** 87–117.

Hwang, P. A., and O. H. Shemdin, 1988: The dependence of sea surface slope on atmospheric stability and swell conditions. *J. Geophys. Res.,* **93** (C11), 13 903–13 912.

Kitaigorodskii, S. A., 1970: *The Physics of Air–Sea Interaction.* Hydrometeoizdat, 284 pp. (Translated from Russian by A. Baruch, Israel Program for Scientific Translations, Jerusalem, 1973, 273 pp.)

Kropfli, R. A., and S. F. Clifford, 1996: The Coastal Ocean Probing Experiment: Further studies of air–sea interaction with remote and in situ sensors. *Proc. IGARSS'96,* Lincoln, NE, Institute of Electrical and Electronics Engineers, 1739–1741.

——, L. A. Ostrovsky, T. P. Stanton, E. A. Skirta, A. N. Keane, and V. Irisov, 1999: Relationships between strong internal waves in the coastal zone and their radar and radiometric signatures. *J. Geophys. Res.,* **104** (C2), 3133–3148.

Li, P. Y., D. Xu, and P. A. Taylor, 2000: Numerical modelling of turbulent airflow over water waves. *Bound.-Layer Meteor.,* **95,** 397–425.

Liu, A. K., C. Y. Peng, B. Chapron, E. Molo-Christensen, and N. E. Huang, 1995: Direction and magnitude of wind stress over wave groups observed during SWADE. *Global Atmos. Ocean Syst.,* **3,** 175–194.

Mahrt, L., D. Vickers, J. Howell, J. Højstrup, J. M. Wilczak, J. Edson, and J. Hare, 1996: Sea surface drag coefficients in the Risø Air Sea Experiment. *J. Geophys. Res.,* **101** (C6), 14 327–14 335.

——, ——, J. Sun, N.-O. Jensen, H. Jørgensen, E. Pardyjak, and H. Fernando, 2001: Determination of the surface drag coefficient. *Bound.-Layer Meteor.,* **99,** 249–276.

Makin, V. K., and V. N. Kudryavtsev, 1999: Coupled sea surface–atmosphere model. 1. Wind over waves coupling. *J. Geophys. Res.,* **104** (C4), 7613–7623.

Makova, V. I., 1975: Features of the dynamics of turbulence in the marine atmospheric surface layer at various stages in the development of waves. *Izv. Acad. Sci. USSR, Atmos. Oceanic Phys.,* **11,** 177–182.

Miller, S., C. Friehe, T. Hristov, and J. Edson, 1997: Wind and turbulence profiles in the surface layer over ocean. Preprints, *12th Symp. on Boundary Layers and Turbulence,* Vancouver, BC, Canada, Amer. Meteor. Soc., 308–309.

Ostrovsky, L. A., J. E. Hare, A. Smirnov, R. A. Kropfli, K. Naugolnykh, E. Skirta, and T. P. Stanton, 1999: The action of swell and internal waves on short surface waves: In situ and radar observations. *Proc. Symp. on the Wind-Driven Air–Sea Interface. Electromagnetic and Acoustic Sensing, Wave Dynamics and Turbulent Fluxes,* M. L. Banner, Ed., Sydney, Australia, UNSW Press, 391–398.

Otto, W. D., J. E. Hare, R. J. Hill, and C. W. Fairall, 1998: The effect of ocean internal waves on the atmospheric surface layer. NOAA Tech. Memo. ERL ETL-293, Boulder, Colorado, 68 pp. [Available from the National Technical Information Service, 5285 Port Royal Rd., Springfield, VA 22061.]

Phillips, O. M., 1977: *The Dynamics of the Upper Ocean.* 2d ed. Cambridge University Press, 336 pp.

Pierson, W. J., Jr., and L. Moskowitz, 1964: A proposed spectral form for fully developed wind seas based on the similarity theory of S. A. Kitaigorodskii. *J. Geophys. Res.,* **69** (24), 5181–5190.

Quanduo, G., and G. Komen, 1993: Directional response of ocean waves to changing wind direction. *J. Phys. Oceanogr.,* **23,** 1561–1566.

Remy, F., and J. P. Giovanangeli, 1999: Wind stress over simulated complex sea states. *Proc. Symp. on the Wind-Driven Air–Sea Interface. Electromagnetic and Acoustic Sensing, Wave Dynamics and Turbulent Fluxes,* M. L. Banner, Ed., Sydney, Australia, UNSW Press, 337–344.

Rieder, K. F., 1997: Analysis of sea-surface drag parameterization in open ocean conditions. *Bound.-Layer Meteor.,* **82,** 355–377.

——, and J. A. Smith, 1998: Removing wave effects from the wind stress vector. *J. Geophys. Res.,* **103** (C1), 1363–1374.

——, and R. A. Weller, 1994: Observed directional characteristics of the wind, wind stress, and surface waves on the open ocean. *J. Geophys. Res.,* **99** (C11), 22 589–22 596.

——, ——, and ——, 1996: Some evidence of colinear wind stress and wave breaking. *J. Phys. Oceanogr.,* **26,** 2519–2524.

Rufenach, C. L., J. J. Bates, and S. Tosini, 1998: *ERS-1* scatterometer measurements—Part 1: The relationship between radar cross section and buoy wind in two oceanic regions. *IEEE Trans. Geosci. Remote Sens.,* **36,** 603–622.

Smedman, A.-S., M. Tjernström, and U. Högström, 1994: Near-neu-

tral marine atmospheric boundary layer with no surface shearing stress: A case study. *J. Atmos. Sci.,* **51,** 3399–3411.

Smith, S. D., 1980: Wind stress and heat flux over ocean in gale force winds. *J. Phys. Oceanogr.,* **10,** 709–726.

——, C. W. Fairall, G. L. Geernaert, and L. Hasse, 1996: Air–sea fluxes: 25 years of progress. *Bound.-Layer Meteor.,* **78,** 247–290.

Stewart, R. H., 1970: Laboratory studies of the velocity field over deep-water waves. *J. Fluid Mech.,* **42,** 733–754.

Sullivan, P. P., J. C. McWilliams, and C.-H. Moeng, 2000: Simulation of turbulent flow over idealized water waves. *J. Fluid Mech.,* **404,** 47–85.

Townsend, A. A., 1972: Flow in a deep turbulent boundary layer over a surface distorted by water waves. *J. Fluid Mech.,* **55,** 47–85.

Wetzel, S. W., 1996: An investigation of the wave-induced momentum flux through phase averaging of open ocean wind and wave fields. M.S. thesis, Joint Program in Applied Ocean Physics and Engineering, Massachusetts Institute of Technology and Woods Hole Oceanographic Institution, 93 pp.

Wilczak, J. M., S. P. Oncley, and S. A. Stage, 2001: Sonic anemometer tilt correction algorithms. *Bound.-Layer Meteor.,* **99,** 127–150.

Zemba, J., and C. A. Friehe, 1987: The marine atmospheric boundary layer jet in the coastal ocean dynamics experiment. *J. Geophys. Res.,* **92** (C2), 1489–1496.